Arch. Mech., **51**, 6, pp. 745–784, Warszawa 1999

Deformation behaviour of TiNi shape memory alloy undergoing R-phase reorientation in torsion-tension (compression) tests

B. RANIECKI ([1]), S. MIYAZAKI ([2]), K. TANAKA ([3]),
L. DIETRICH ([1]) and C. LEXCELLENT ([4]),

([1]) *Polish Academy of Sciences*
Institute of Fundamental Technological Research,
Świętokrzyska 21, 00–049 Warsaw, Poland
E-mail: braniec@ippt.gov.pl

([2]) *University of Tsukuba, Japan*

([3]) *Tokyo Metropolitan Institute of Technology, Hino/Tokyo, Japan*

([4]) *LMARC-UMR CNRS 6604 UFR Sciences, Besançon, France*

THE DEFORMATION BEHAVIOUR associated with the R-phase reorientation is investigated in a Ti-51.0 at%Ni polycrystalline shape memory alloy under the torsion-tension (compression) stress state, and special theoretical framework is developed to describe the observed alloy performance. The limit condition to start the reorientation process, represented as a surface on the axial stress-shear stress plane, is determined for the proportional loading path. The result is well described, not by the Huber-Mises condition (the J_2-theory) but by the model (the J_3-theory), by taking into account the third invariant of stress deviator through the concept of the shape function. The values of the shape function are determined experimentally. The basic experimental features of the deformation in the R-phase, such as the flow rule, the ratios of the reorientation strain rates and the dimensionless ratio of the reorientation work, are compared with the predictions of theories that neglect the effects of pressure, compressibility of reorientation strains and effects of induced anisotropy. The J_3-theory turns out to be more realistic than the J_2-theory.

Keywords: TiNi shape memory alloy, Multiaxial stress state, Torsion-tension (compression) test, Reorientation of R-phase, Stress-induced R-phase, Limit surface to start reorientation.

1. Introduction

CURRENT APPLICATIONS of shape memory alloys (SMAs) look to progress simultaneously and rapidly along the different directions of "downsizing", "upsizing" and "compositization". Thin films of the order of μm in thickness, which exhibit

http://rcin.org.pl

almost perfect shape memory effect have been developed, and are regarded as a potential candidate material to drive micromachines [1 – 3]. Development of thin films showing stable shape memory effect associated with both the R-phase and martensitic transformations are still an urgent task in current metallurgy. On the other hand, larger SMA devices, of the order of 10 cm or larger in size, are increasingly required, being expected to carry mechanical loads while exhibiting shape memory effect. Fasteners of the pipes are a successful example realized by advanced Fe-based SMAs [4]. SMAs are favorably employed as a component material to form a composite with a matrix material [5 – 7]. The composites are expected to perform, as a smart material, a special function, which is impossible to be performed by any single material. Among such competitors as the piezoelectric materials, the electrorheological fluids and the electrostrictive/magnetostrictive materials, SMAs dominate in producing larger driving force and stroke. The way of cooling is, however, always the point of special consideration, especially when a high speed response is expected of the composite.

In all these applications, SMAs are in action under not a simple uniaxial stress state but a complicated multiaxial stress state, and in addition, the non-isothermal state in both space and time is the usual case. Alloy performance under such complicated thermomechanical situation should, therefore, be fully clarified both experimentally and theoretically, from the point of view of both metallurgy and thermomechanics. On the theoretical side, starting from FALK [8, 9] and TANAKA [10, 11], many attempts have been made to establish unified frameworks governing the transformation and deformation phenomena in SMAs [12 – 28]. The work by RANIECKI *et al.* should especially be mentioned for its sound base on thermodynamics and subsequent wide applicability [29 – 32]. The transformation driving force was rationally formulated in close relation to the second law of thermodynamics, and the transformation kinetics was introduced consistently. The micromechanical study by PATOOR *et al.* [33] and the thermomechanical FEM modelling by FISCHER [34] should also be worth remarking since they have established each methodology in transformation thermomechanics in SMAs.

Huge amount of experiments have been carried out in many SMAs under uniaxial stress state, accumulating data on the stress-strain-temperature hysteresis, the propagation of phase interface, the transformation conditions, and so on, both static and cyclic conditions [2, 35 – 36]. These results helped a lot to establish and refine the theories, and to identify the material parameters. For example, the knowledge on the transformation zones in the stress-temperature space, only in which the transformations progress, has presented a clear picture about the thermomechanical behaviour of SMAs, and driven the establishment of the theories based on it [11, 37 – 40]. The concept of the transformation zone finally leads to the transformation start/finish conditions represented by the surfaces

http://rcin.org.pl

in the general stress-temperature space, which is similar to the yield surface in plasticity [41]. The observation of asymmetry of stress-strain curves has stimulated the study of the transformation work dissipated during transformation; its path-independence is the point of discussion [42, 43].

Under the multiaxial stress state, however, few experimental results have been reported in the martensitic transformation range by SITTNER and TOKUDA [44 – 46] and ROGUEDA *et al.* [47] in Cu-based SMA, NISHIMURA *et al.* [48, 49] in Fe-based SMA and SEHITOGLU *et al.* [50, 51] in TiNi and Cu-based SMAs. Some points to remark: Asymmetry of the martensitic transformation start surface in the stress-temperature space was clearly observed in all SMAs, thus approving the theory with the third invariant of stress tensor [16], which has been suggested in the micromechanical investigation by PATOOR *et al.* [52]. The normality rule was shown to be acceptable, though a full conclusion should be made after further accumulation of data.

Usually a series of thermomechanical loads is applied to the specimen prior to the tests in order to acquire a stable response of the specimen. The process is called the training [53]. This means that the test results might not be the intrinsic response of the alloy, but be an apparent behaviour strongly influenced by the type of training employed. In order to study precisely the intrinsic property of the alloy, one has to carefully prepare the alloy specimen so that it exhibits, without any type of training, enough stable response in the whole course of tests.

In TiNi SMAs the R-phase transformation occurs in a certain temperature range just prior to the martensitic transformation [1, 54 – 56]. The rhombohedral phase is produced from the parent B2 phase during the transformation. The stress-strain curve changes its form from apparent plasticity to pseudoelasticity depending on the test temperature; the former is the shape memory effect exhibiting the recoverable deformation, whereas in the latter, the stress-induced pseudoelasticity is associated with the stress-induced forward and reverse transformations. In almost all cases, the pseudoelasticity is observed in a relatively narrow temperature range without showing any large hysteresis. This is the reason why the R-phase transformation is preferably used in shape memory devices requiring a sensitive response to the input.

Metallurgy tells us that the R-phase transformation starts during thermomechanical loading when a transformation start condition is satisfied, and finishes when a transformation-finish condition is fulfilled, forming the twin related R-phase variants. The twinned structure is self-accommodated under the stress-free state and is preferred by the applied stress, as in the case of the martensitic transformation. The lattice distortion in the R-phase and/or the variants reorientation of the twinned variants then follow in the subsequent thermomechanical loading. At higher stress and higher temperature range, after the preceding R-phase transformation, the usual martensitic transformation follows [35].

http://rcin.org.pl

In this paper, as in the first report by the same authors on the comprehensive behavior of TiNi SMA under multiaxial stress state, the experimental results in the R-phase transformation is presented under torsion-tension (compression) stress state. A Ti-50.1%at.Ni SMA was specially prepared for the tests; details of the alloy preparation is reported elsewhere [57]. Special attention is focused on the limit surface to start the reorientation process and the hysteresis loops. A continuum mechanical approach is proposed to model the behaviour of R-phase.

After the experimental and theoretical preliminaries are explained in Sec. 2, Section 3 is devoted to the reorientation (detwinning) plasticity of the pre-existing R-phase, and in the forthcoming paper by the same authors the R-phase pseudoelasticity associated with the stress-induced R-phase transformation will be investigated.

2. Preliminaries

2.1. Alloy, experimental apparatus and experimental procedures

The alloy tested is a Ti-51.0at%Ni polycrystalline SMA, which was annealed at 673 K for 3.6 ks after solution treatment. Transformation temperatures, determined by means of DSC (differential scanning calorimetry) tests, are as follows:

R-phase transformation

$$Rs = 306\ K, \quad Rf = 293\ K,$$
$$RAs = 305\ K, \quad RAf = 316\ K.$$

Martensitic transformation

$$Ms = 253\ K, \quad Mf = 208\ K,$$
$$As = 268\ K, \quad Af = 306\ K.$$

Fundamental thermomechanical properties are presented in Ref. [57] together with some preliminary data of the alloy performance.

It is, nevertheless, necessary to emphasize here that the alloy was designed, by both adjusting the composition and selecting an appropriate heat treatment, to realize a very stable response to thermomechanical loading. The specimen can, as a result, be used repeatedly without any fear of accumulating some irreversible structural change on the microscopic scale. The thermomechanical training is not necessary at all. It should be stressed that all tests reported here were carried out with a single specimen. Actually the initial distance between two marks on the surface of the specimen, 65.815 mm, and the initial rotation of the line connecting the marks with respect to the specimen axis, $-0°18'$, were changed

http://rcin.org.pl

only by 0.02 mm and 0°06′ respectively, after 46 times of thermomechanical loading/unloading to get all data shown in this paper.

The thin-walled tubular specimen, 19 mm in outer diameter, 16 mm in inner diameter and 122 mm in length, is illustrated in Fig. 1. After machining, the specimen was etched by acid solution. The design considerations on the wall-thickness were dictated by avoiding buckling in compression and a small enough thickness/outside-diameter ratio so that the wall may be considered as thin.

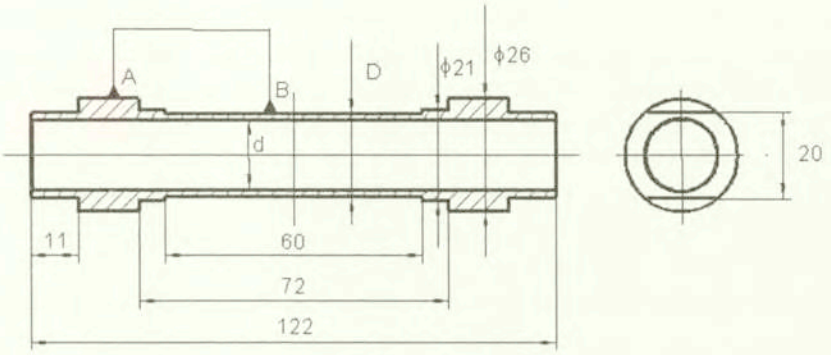

FIG. 1. Test specimen.

A servohydraulic Instron 1343 axial-torsion load frame, together with an MTS TestStar^{TM} II fully digital controller, was used for the computerized testing and data acquisition. The maximum axial and torsion load capacities are rated at ±100 kN and ±1000 Nm, respectively. Two separate servo-control channels of the TestStar^{TM} II controller connected to a PC computer of the system can independently apply controlled axial load and torque. The axial stress (σ_z) and the shear stress (τ) were determined from the output of the axial and torsion loadcells, and were controlled proportionally under isothermal conditions (for details, see Sec. 2.2). The stress rate was kept constant to 1 MPa/sec during the whole tests.

The testing machine recorded, on a hard disk of the PC computer, 8 channels of data. The axial stress (σ_z) and the shear stress (τ) are the controlled quantities, whereas the axial strain (ε_z), the shear strain ($\varepsilon_{z\theta}$) and the hoop strain (ε_θ) represent the response of the specimen. The radial component ε_r was undetermined.

Tests were carried out at constant temperatures in the range 260 K to 315 K. The temperature of the specimen was increased/decreased using an Instron chamber. Temperature inside the chamber was controlled within ±0.5 K at demanded level using Instron controller type 3110. Temperature at upper and lower part of the specimen gauge length was also measured during the test by two K-type (chromel-alumel) thermocouples connected to microprocessor based thermometer

http://rcin.org.pl

model 502. Temperature differences at the measuring points were less than 1 K during the whole loading-unloading process for a given path of loading.

Axial, hoop and shear strains were measured by uniaxial and rosette-type strain gages cemented in the middle part of a specimen. Two 45° rosettes EP-08-125RA-120 by Micro-Measurements, bonded to the outer surface of the specimen and located diametrically opposed to each other, were wired in full bridge circuit with four active gauges for shear strain measurement. The third strain gauge of each rosette, aligned with longitudinal axis of the specimen, and two additional separate strain gauges for temperature compensation, located on a specially designed semi-ring, were wired in full bridge circuit with two active gauges for axial strain measurements. The hoop strain was measured by means of the additional two strain gauges, bonded to the specimen and located also diametrically opposed to each other. Two strain gauges (all Micro-Measurements type EP-08-125DQ-120) were bonded on the surface of the semi-ring for the temperature compensation. The gauges were wired in half bridge circuit and consist of two active and two passive elements.

Load and torque transmission is affected by specially designed grips assuring load axiality and backlash elimination, thus enabling us to perform cyclic, reverse loading of the specimen.

More details concerning the experimental procedure are given in Ref. [58].

For the tests in reorientation (detwinning) plasticity of the pre-existing R-phase, the test temperature was kept constant during tests at $T = 260$ K, 280 K, 300 K, whereas the following temperature ranges in the pseudoelasticity associated with B2 (Austenite) $\rightarrow$ R phase transformation will be selected in the forthcoming paper: $T = 310$ K, 311.5 K, 315 K, 322.5 K.

Prior to a series of test, composed of isothermal proportional loading up to a maximum stress state and subsequent unloading, the specimen is heated up to 340 K and cooled down to the test temperature. This process fully erased the macroscopic permanent strain induced in the preceding test, and assured that the temperature-induced R-phase is the only phase to exist when the test starts at the reorientation temperature range, and that only the parent B2 phase exists when the tests start at higher pseudoelastic temperature range.

2.2. Controlled quantities

Suppose $\sigma_{ij}(t)$ represents a time history of the stress tensor. The loading path is generally identified as follows:

$$\sigma_{ij}(t) = \sigma_{ij}^{\max} \frac{t}{t_{\max}},$$

where $\sigma_{ij}^{\max}$ represents the maximum value of the stress tensor σ_{ij} at the last moment of loading $t_{\max}$. Both parameters are constant in the proportional loading

http://rcin.org.pl

tests. If the deviatoric stress tensor

$$S_{ij}(t) = \sigma_{ij}(t) - \frac{1}{3}\delta_{ij}\sigma_{mm}$$

is introduced, the proportional loading path can be rewritten by

$$S_{ij}(t) = S_{ij}^{\max}\frac{t}{t_{\max}}; \qquad \mathbf{S}^{\max} \equiv \operatorname{dev}(\sigma^{\max}) = \text{const.}$$

or in the equivalent form by

$$\sigma_{ef} \equiv \left(\frac{3}{2}S_{ij}S_{ij}\right)^{1/2} = \overline{\sigma}_{\max}\frac{t}{t_{\max}},$$

$$(\overline{\sigma}_{\max})^2 = \frac{3}{2}S_{ij}^{\max}S_{ij}^{\max} = \text{const.}$$

The effective stress σ_{ef} defined above is used in the whole course of this study to measure the extent of load state under multiaxial stresses. The stress rate $\overline{\sigma}_{\max}/t_{\max}$ was kept constant 1 MPa/sec during the whole tests.

In this study, Torsion + Tension (Compression) tests of thin-walled tubular specimen are often investigated from the theoretical point of view, and are actually carried out in TiNi alloy specimen. The class of the tests is simply called the "A-experiments" in the following discussion.

In A-experiments, the above formulae are reduced to as follows: Defining non-zero components of stress tensor by

$$\sigma_z \Leftrightarrow \sigma_{11} \quad \text{(axial stress)} \quad \text{and} \quad \tau \Leftrightarrow \sigma_{12} = \sigma_{21} \quad \text{(shear stress)},$$

one obtains

$$\sigma_{ef} = \overline{\sigma} = \sqrt{\sigma_z^2 + 3\tau^2} = (\operatorname{sign}\sigma_z)\sigma_z\sqrt{1+3m^2}, \tag{2.1}$$

where the path parameter m is defined by

$$m = \frac{\tau}{\sigma_z}. \tag{2.2}$$

Tests along five proportional paths, illustrated in Fig. 2, were performed at each temperature. These paths are identified by means of the parameter y (cf. Sec. 2.3) or m as follows:

Path #1	Simple shear	$i = 1$,	$m = \infty$,	$y = 0$,
Path #2	Simple tension	$i = 2$,	$m = 0$,	$y = 1$,
Path #3	Simple compression	$i = 3$,	$m = 0$,	$y = -1$,
Path #4	Proportional tension and shear ($\tau = \sigma_z$)	$i = 4$,	$m = +1$,	$y = 11/16$,
Path #5	Proportional compression and shear ($\tau = -\sigma_z$)	$i = 5$,	$m = -1$,	$y = -11/16$,

http://rcin.org.pl

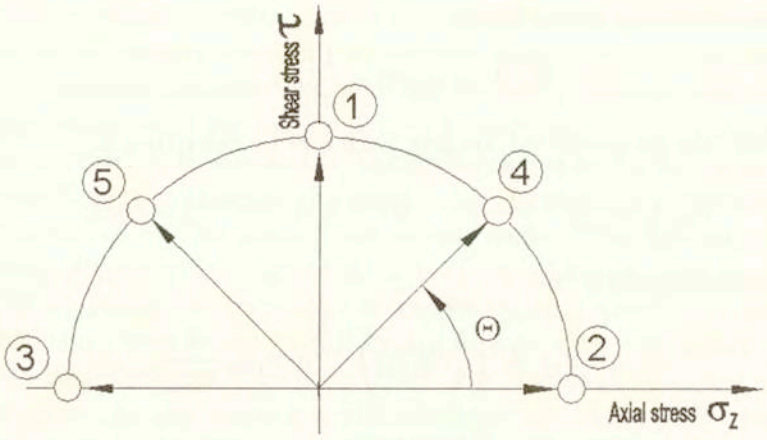

FIG. 2. Loading paths.

2.3. Path characteristics

In order to take rationally into account the path-dependence of the alloy behaviour, the y-function or y-parameter is introduced by

$$y(\sigma_{ij}) \equiv 3\sqrt{6}\frac{J_3'}{(J_2')^{3/2}}$$

(2.3)

$$J_2' \equiv \frac{2}{3}\sigma_{ef}^2 = S_{ij}S_{ij}, \qquad J_3' \equiv \det S_{ij} = \frac{1}{3}\mathrm{tr}(\mathbf{S})^3$$

where J_2' and J_3' denote the second and the third invariants of the stress deviator, respectively. Note that the y-parameter is homogenous of order zero in the stress tensor $\mathbf{S}$, and $-1 \leq y \leq 1$. Moreover, $y = \text{const.}$ during proportional loading.

It should be remarked that J_3' was favorably employed when elaborating the effect of loading path on the plastic behaviour in isotropic materials. PATOOR *et al.* have shown, through the micromechanical investigation, that the case is also true in thermomechanical behaviour of Cu-based SMA [52]. Raniecki and Lexcellent have recently introduced the y-function in the transformation thermomechanics to explain the limit surface of martensitic transformation in Cu-based SMA [16].

In the case of A-experiments, the parameter y reads as

$$y = \frac{\sigma_z(2\sigma_z^2 + 9\tau^2)}{2(\sigma_z^2 + 3\tau^2)^{3/2}} = (\mathrm{sign}\sigma_z)\frac{2 + 9m^2}{2(1 + 3m^2)^{3/2}} \tag{2.4}$$

the value of which is listed for each loading path in the table above.

http://rcin.org.pl

It is worth noting the relation between the Lode-parameter μ_L and y introduced here

$$y = \frac{\mu_L(3-\mu_L)(3+\mu_L)}{(3+\mu_L^2)^{3/2}}\text{sign}(\sigma_2-\sigma_1) \tag{2.5}$$

or alternatively

$$\mu_L = -\sqrt{3}\text{tg}\theta; \qquad y = -\sin 3\theta$$

where θ stands for the angle of vector-radius on octahedral plane. In the course of proportional A-experiments the parameter y and the angle θ remains constant. Moreover, the principal axis does not rotate. There is a simple relation between the angle θ and the angle α that determines the orientation of the principal axis with respect to the z-axis,

$$\sqrt{3}\text{tg}\theta = \text{sign}(\sigma_z)|\cos(2\alpha)|, \qquad |\cos(2\alpha)| = \frac{1}{\sqrt{1+4m^2}}$$

2.4. Remarks

i) Recall that the stress paths $\sigma'(t)$ and $\sigma(t)$ connected by

$$\boldsymbol{\sigma}'(t) = \mathbf{R}^T\boldsymbol{\sigma}(t)\mathbf{R}, \quad \text{where } \mathbf{R}^T\mathbf{R} = \mathbf{1}, \quad \mathbf{R} \neq \mathbf{1} \text{ and } \det\mathbf{R} = 1,$$

are equivalent in the sense that if a physical property $\varphi(\boldsymbol{\sigma})$ is such that $\varphi(\boldsymbol{\sigma}) = \varphi(\boldsymbol{\sigma}')$ for arbitrary $\mathbf{R}$, then the specimen is isotropic with respect to the property φ. It can be shown that in the class of A-experiments there exists no two distinct proportional and equivalent paths. This makes certain problem as regards direct verification of an isotropy postulate. The anisotropy effects can be estimated only in indirect way, e.g., by confronting the conclusions following from the most general representations of the isotropic functions with the experimental facts.

ii) Likewise, the effect of hydrostatic stresses cannot be estimated directly in the A-experiments.

iii) In the A-experiments one can produce neither "tensile" ($\sigma_1 > 0$, $\sigma_2 > 0$) nor "compressive" ($\sigma_1 < 0$, $\sigma_2 < 0$) stress states, where σ_1 and σ_2 are the principal stresses ($\sigma_3 = 0$).

3. Reorientation Plasticity of R-phase

The reorientation processes of the pre-existing R-phase progress, not only in the present SMA but also in almost all TiNi SMAs, under low applied stresses at specific temperature range [54 – 56]. The detwinning of the R-phase variants is the mechanism of deformation under the applied stress, meaning the processes are highly dependent on the stress path. The low total strains of the order of

http://rcin.org.pl

10^{-3}, at most $\varepsilon < 10^{-2}$, are induced, and the permanent strains amount to the order of $10\times$(typical elastic strain).

Experimental results are presented below, together with the way of data processing. A model of reorientation plasticity of R-phase is also discussed.

3.1. Actual loading paths

In the tests the maximum stresses

$$\sigma_{ef}(A,i) = \max_t \sigma_{ef}(t,i); \qquad (i = 1,2,3,4,5),$$

a)

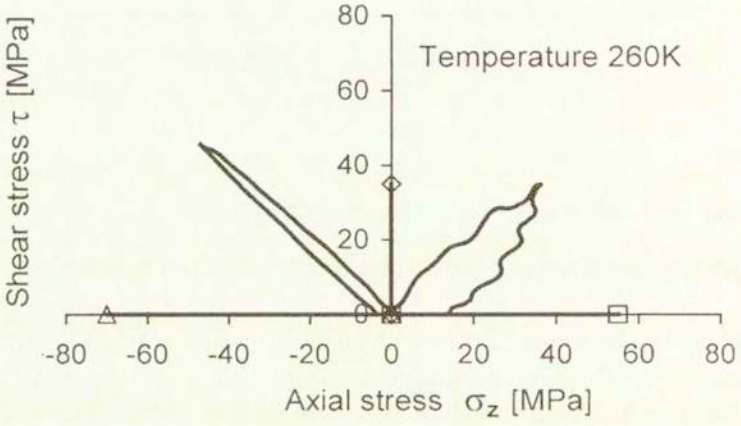

b)

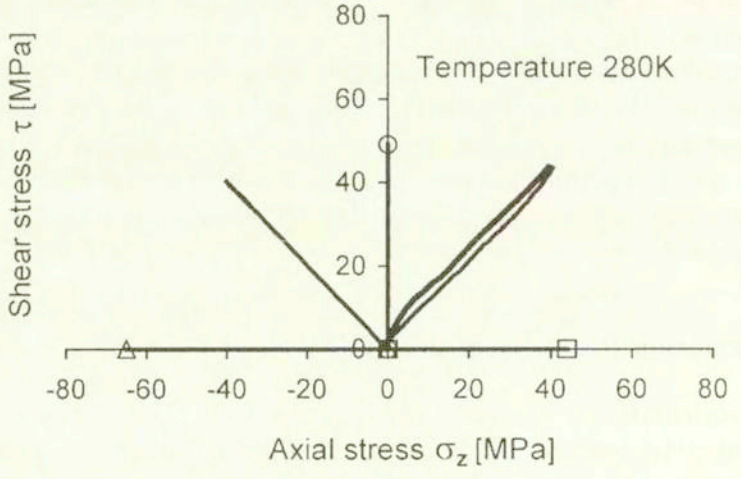

[FIG. 3 a, b]

http://rcin.org.pl

c)

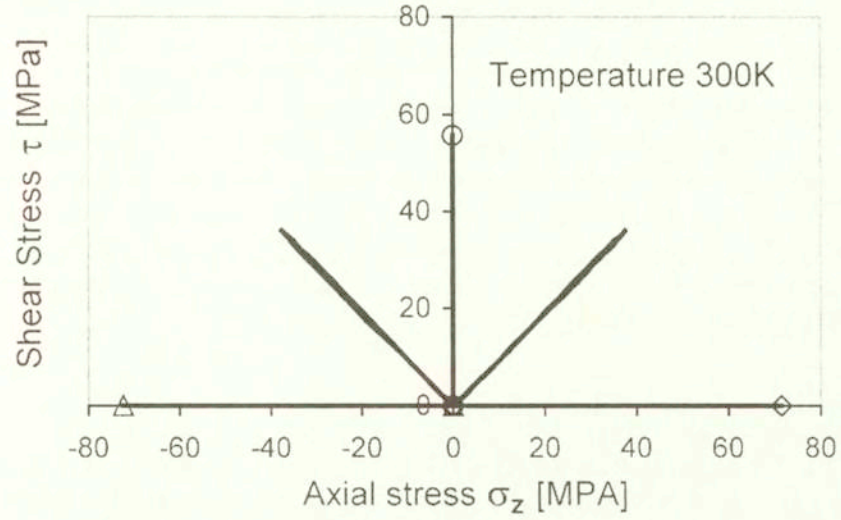

FIG. 3. Actual loading paths at; a) 260 K, b) 280 K and c) 300 K.

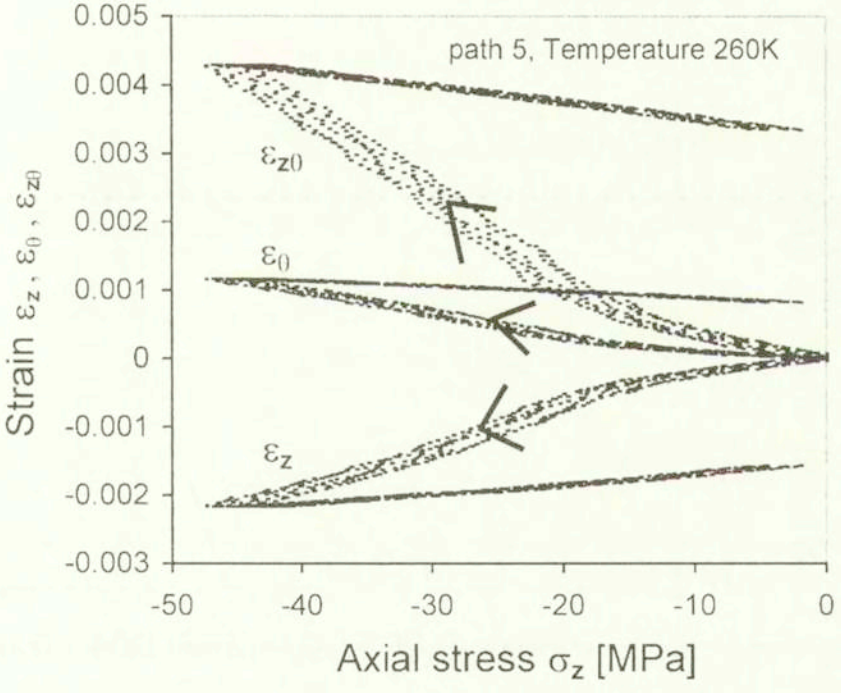

FIG. 4. An example of "on-line" stress-strain response for Path #5 at 260 K.

http://rcin.org.pl

were different for the different path i and the test temperature T, and moreover the actual paths were not exactly proportional in some cases, as shown in Fig. 3 at different temperatures. The maximum stress was set as low as possible so that no irreversible microstructural change was accumulated in the specimen, but at the same time as high as possible so that the critical stress to start the reorientation process and the elastic modulus can be determined accurately enough (cf. Fig. 6 later). Loading is not exactly controlled by either a common stress amplitude or a common strain amplitude.

3.2. Illustration of recorded data

The typical "on-line" data for Path #5 at 260 K are shown in Fig. 4. After the initial response, characteristic behaviour in the reorientation (detwinning) process, in which the temperature-induced, self-accommodated, R-phase variants are reoriented to a favorable one during mechanical loading. The obtained on-line data were smoothed by means of two methods; the "average mean" and the "polynomial fit". The deviation of the raw data from the smoothed stress-strain curves were small enough; $|\Delta\sigma_{ij}| \leq 2$ MPa, $|\Delta\varepsilon_{ij}| \leq 5 \cdot 10^{-5}$, as can be seen from Fig. 5a,b.

a)

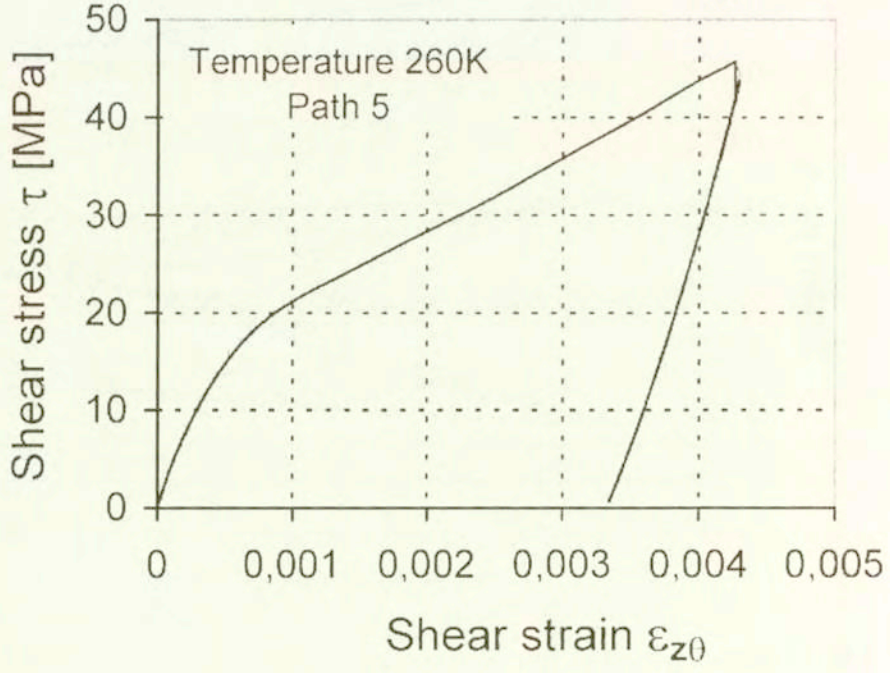

[FIG. 5 a)]

http://rcin.org.pl

b)

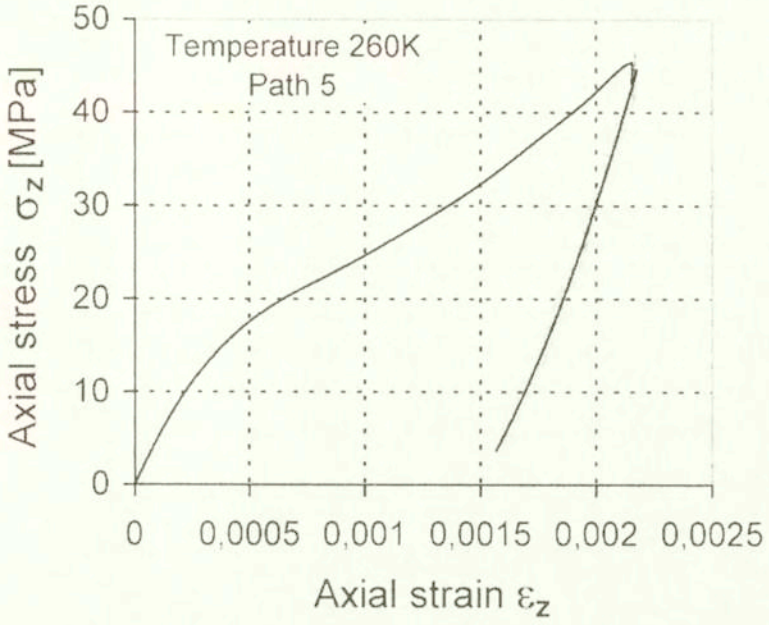

FIG. 5. "On-line data" and "smoothed data" for Path #5 at 260 K; a) $\tau - \varepsilon_{z\theta}$ curve, b) $-\sigma_z - \varepsilon_z$ curve.

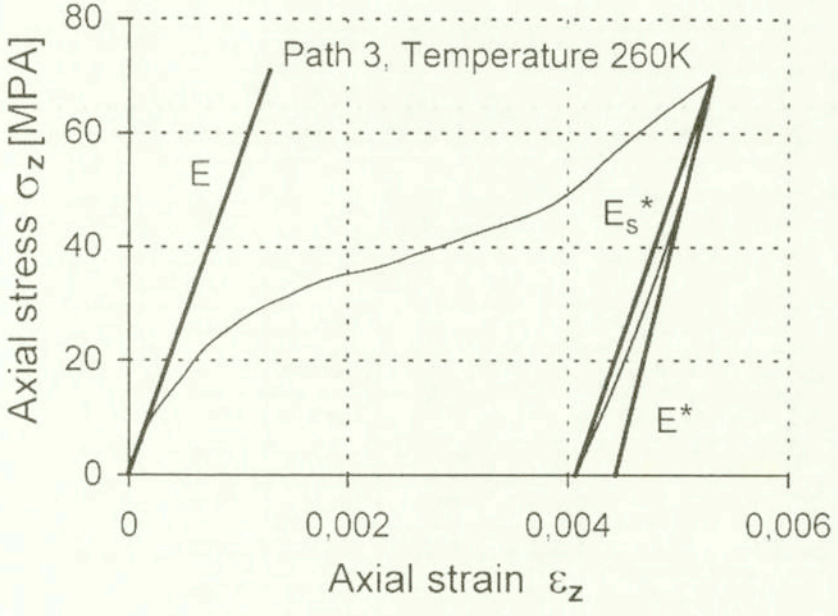

FIG. 6. Definition of elastic contants.

http://rcin.org.pl

3.3. Determination of elastic constants

Elastic moduli E and 2μ were determined at a total strain offset equal to 10^{-4}. On the other hand, the elastic moduli during unloading, having quite different values from E and 2μ, were defined as both the secant moduli E_s^*, $2\mu_s^*$ and the tangential moduli E^*, $2\mu^*$ (cf. Fig. 6 illustrating the data for Path #3 at 260 K).

For Paths #2 and #3, Poisson's ratio was calculated by means of the isotropic relation $\nu = E/2\mu - 1$ with the shear modulus identified for Path #1. All these elastic moduli exhibit strong temperature-dependence, as tabulated in Table 1.

Table 1. Elastic constants at; a) 260 K, b) 280 K and c) 300 K.

a) Elastic constants; $T = 260$ K

	PATH Number				
	1	2	3	4	5
2μ MPa	43186.5	–	–	41976.4	44079.4
$2\mu^*$ MPa	43449.4	–	–	44454.8	60019.1
$2\mu_s^*$ MPa	30765.3	–	–	31864.3	46253.7
E MPa	–	51683.1	54489.8	48869.1	50426.2
E* MPa	–	61726.8	78903.3	58771.5	92154.8
$\mathbf{E}_s^*$ MPa	–	38300.5	55493.5	35449.0	68400.9
ν MPa	–	0.1967	0.2617	0.1642	0.1440
ν^* MPa	–	0.4207	0.8160	0.3221	0.5354
ν_s^* MPa	–	0.2449	0.8038	0.1125	0.4788

b) Elastic constants; $T = 280$ K

	PATH Number				
	1	2	3	4	5
2μ MPa	38519.3	–	–	34635.9	33711.3
$2\mu^*$ MPa	48601.8	–	–	43392.9	56736.0
$2\mu_s^*$ MPa	30565.0	–	–	26816.6	39270.8
E MPa	–	47248.3	58338.2	38525.9	41133.3
E* MPa	–	52074.9	78034.8	56423.2	77866.6
$\mathbf{E}_s^*$ MPa	–	31369.3	47724.9	31621.0	52177.7
ν MPa	–	0.2266	0.5145	0.1120	0.2200
ν^* MPa	–	0.0710	0.6060	0.3000	0.3720
ν_s^* MPa	–	0.0260	0.5610	0.1790	0.3280

http://rcin.org.pl

c) Elastic constants; $T = 300$ K

	PATH Number				
	1	2	3	4	5
2μ MPa	31979.5	–	–	32413.2	39823.4
$2\mu^*$ MPa	44659.5	–	–	38503.4	48291.5
$2\mu_s^*$ MPa	29388.8	–	–	24275.3	32711.5
E MPa	–	33465.9	40935.2	41763.8	43538.9
$\mathbf{E}^*$ MPa	–	55909.4	74457.0	50545.0	65466.1
$\mathbf{E}_s^*$ MPa	–	32243.8	48178.0	30057.8	43093.0
ν MPa	–	0.0460	0.2800	0.2880	0.0930
ν^* MPa	–	0.2520	0.6670	0.3130	0.3560
ν_s^* MPa	–	0.0970	0.6390	0.2380	0.3170

3.4. Reorientation (detwinning) strain

The reorientation strain is defined by subtracting the elastic component from the total strain;

$$\varepsilon_{ij} \equiv \varepsilon_{ij} - M_{ijkl}\sigma_{kl} = \varepsilon_{ij} - \varepsilon_{ij}^e,$$

where M_{ijkl} denotes the elastic compliance tensor. Under the reasonable assumptions of the isotropic elastic behaviour and the incompressibility of the reorientation strain, the following strain components have to be considered in the tests:

$$\begin{aligned} \varepsilon_r^T &= -(\varepsilon_\theta^T + \varepsilon_z^T), \\ \varepsilon_z^T &= \varepsilon_z - \sigma_z/E; \qquad \varepsilon_{z\theta}^T = \varepsilon_{z\theta} - \tau/2\mu, \\ \varepsilon_\theta^T &\equiv \varepsilon_\theta + \left(\frac{1}{2\mu} - \frac{1}{E}\right)\sigma_z. \end{aligned} \tag{3.1}$$

The equivalent total strain and the equivalent reorientation strain, defined by

$$\varepsilon_{eq} = \sqrt{\frac{2}{3}\varepsilon_{ij}\varepsilon_{ij}} \qquad \text{and} \qquad \varepsilon_{eq}^T = \sqrt{\frac{2}{3}\varepsilon_{ij}^T\varepsilon_{ij}^T},$$

respectively, can be expressed in the case of A-experiments by

$$\varepsilon_{eq}^T = \frac{2\sqrt{3}}{3}\sqrt{(\varepsilon_z^T - \varepsilon_\theta^T)^2 + 3\varepsilon_z^T\varepsilon_\theta^T + (\varepsilon_{z\theta}^T)^2}. \tag{3.2}$$

Similar definition is employed for the equivalent reorientation strain rate;

$$\dot{\varepsilon}^T \equiv \sqrt{\frac{2}{3}\dot{\varepsilon}_{ij}^T\dot{\varepsilon}_{ij}^T} = \frac{2\sqrt{3}}{3}\sqrt{\left(\dot{\varepsilon}_z^T - \dot{\varepsilon}_\theta^T\right)^2 + 3\dot{\varepsilon}_z^T\dot{\varepsilon}_\theta^T + \left(\dot{\varepsilon}_{z\theta}^T\right)^2}. \tag{3.3}$$

http://rcin.org.pl

In Fig. 7 the reorientation strain tensor components ε_z^T, ε_θ^T and $\varepsilon_{z\theta}^T$ are plotted versus the axial component of stress tensor σ_z for the data given in Fig. 5 (Path #5, 260 K), showing clearly that the elastic components are subtracted.

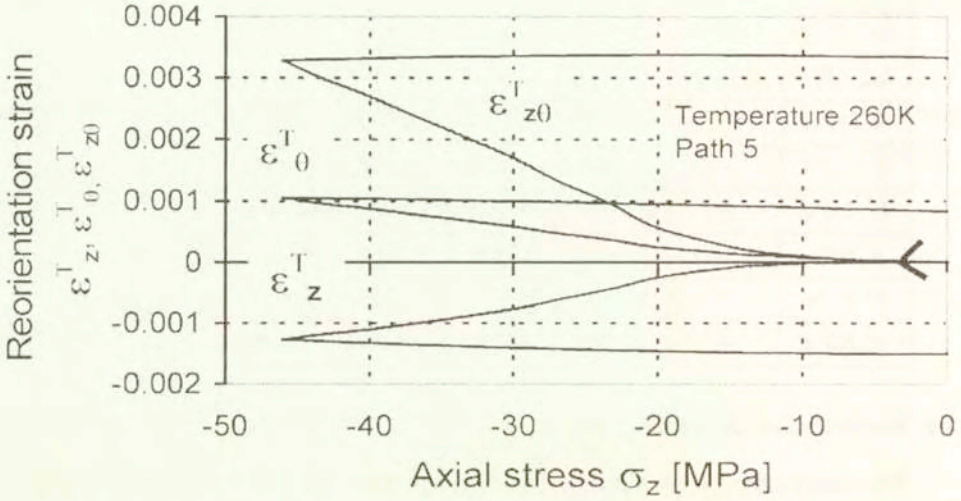

FIG. 7. Stress-reorientation strain curves for Path #5 at 260 K.

3.5. Effective stress - equivalent reorientation strain curves

The isothermal alloy response under torsion-tension (compression) loads can now be plotted on the effective stress-equivalent reorientation strain plane; Figure 8 represents the path-dependence of the curve at each test temperature, whereas in Fig. 9 its temperature-dependence is displayed for each loading path. As was explained in Sec. 3.1, loading is not exactly controlled by either a common stress amplitude or a common strain amplitude.

Figures reveal the strong path-dependence of the response of the specimen to the imposed loading. The effective stress-equivalent reorientation strain curves actually do not converge to a master curve as in von Mises plasticity (J_2-theory). Certain characteristic features of the behaviour can be distinguished:

a) At fixed temperature and fixed effective stress, the induced reorientation equivalent strains in pure shear (Path #1) or combined compression and shear (Path #5) are smaller than in simple tension (Path #2) or in combined tension and shear (Path #4).

b) Under fixed equivalent reorientation strain (geometrical constraint) the recovery effective stress, which could be produced after subsequent heating, are expected to be the highest in simple shear (or combined shear and compression) and the smallest in simple tension.

http://rcin.org.pl

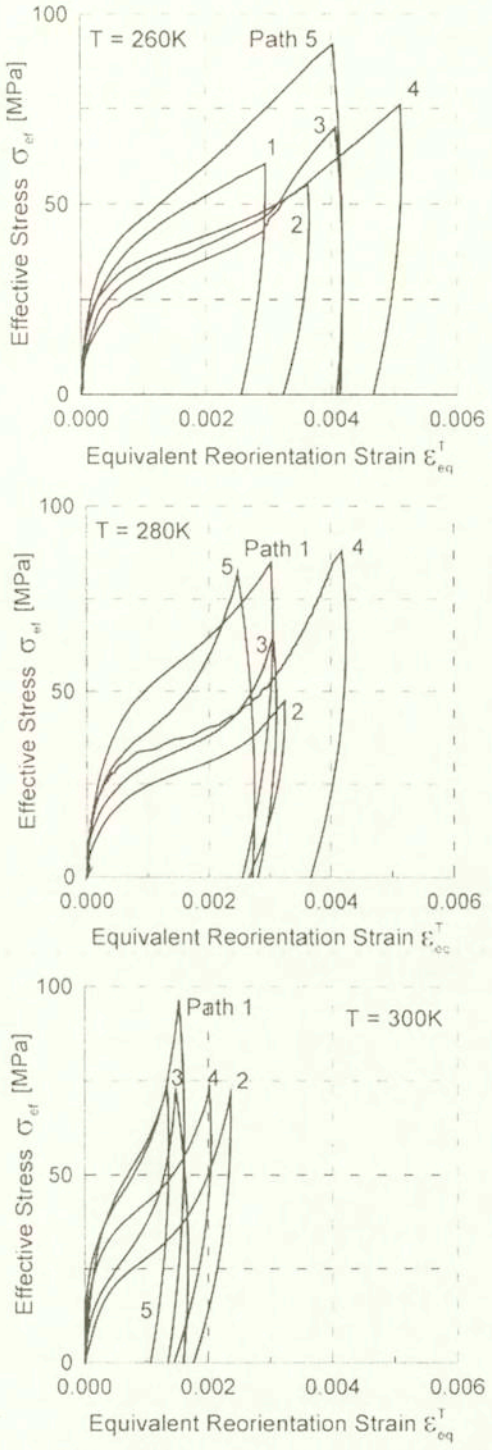

FIG. 8. Effect of loading path on effective stress-equivalent strain curves at: a) 260 K, b) 280 K and c) 300 K.

http://rcin.org.pl

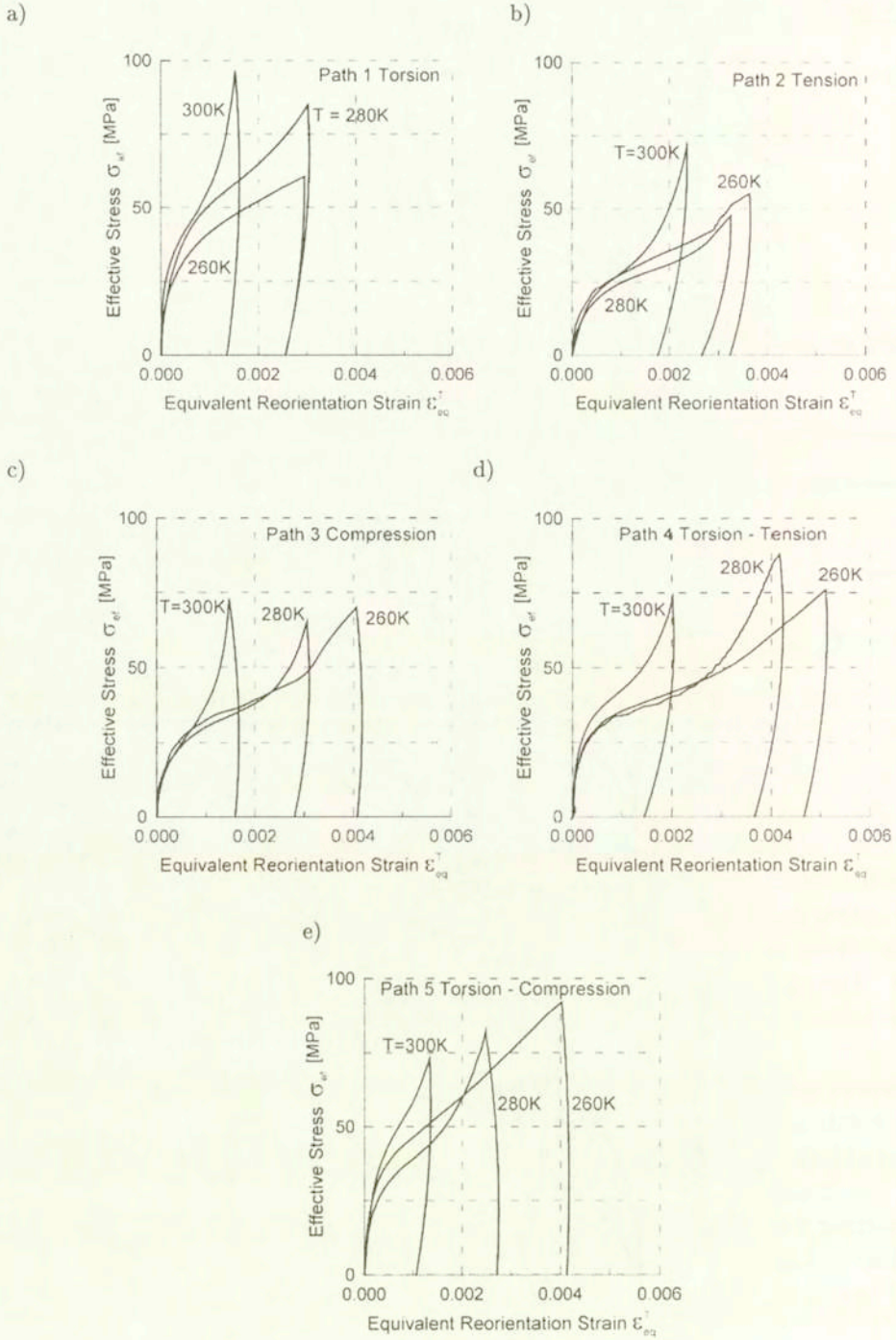

FIG. 9. Effect of temperature on effective stress-equivalent strain curves for: a) Path #1 (torsion), b) Path #2 (tension), c) Path #3 (compression), d) Path #4 (torsion-tension) and e) Path #5 (torsion-compression).

http://rcin.org.pl

c) In accordance with the properties a) and b) above, the rate of reorientation hardening is the highest during torsion or combined torsion and compression.

d) As a rule, the rate of the reorientation hardening is increasing function of the temperature for all paths.

3.6. Limits of initial reorientation - Limit surface of reorientation

The stress-strain curves in Figs. 8 and 9 clearly show that the reorientation process starts at a critical stress, which depends on both the temperature and the loading path. By having always in mind the analogy to the yield stress and the yield surface in plasticity, the critical stress to start the reorientation process is discussed in this section.

3.6.1. Definition of critical stress. Let us denote the critical value of effective stress for path i by σ^T, and different operational definitions are introduced here (Fig. 10) illustrates them for data of Path #5 at 260 K.);

σ_1^T – Critical stress determined by means of the strain offset 10^{-4},

σ_2^T – Critical stress determined by means of the strain offset 2×10^{-4},

σ_3^T – Critical stress determined as an intersection of tangent line with the σ_{ef}-axis.

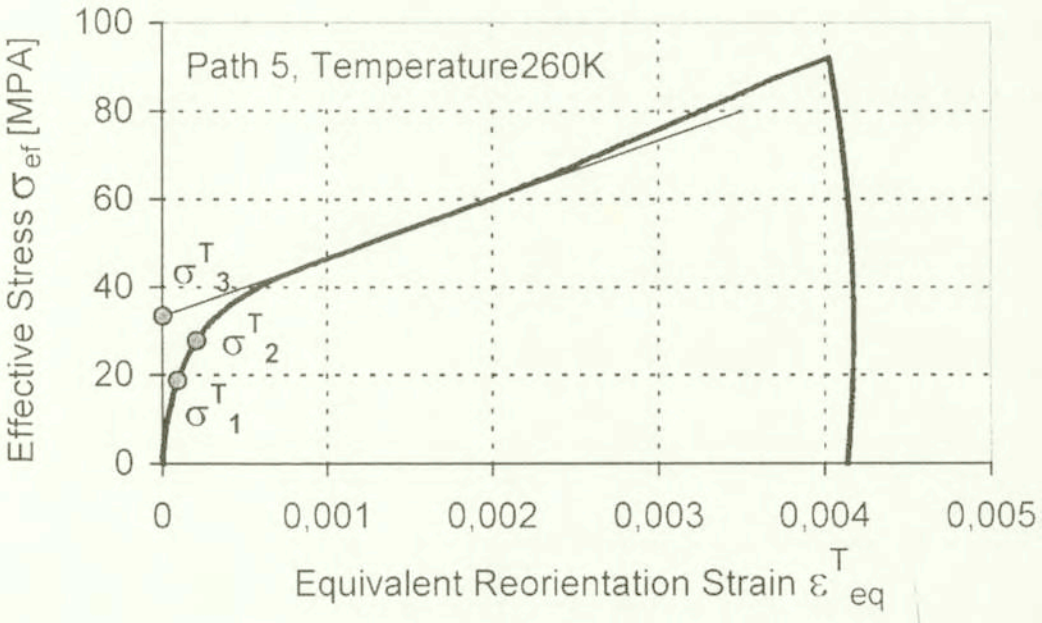

FIG. 10. Definition of critical stress.

http://rcin.org.pl

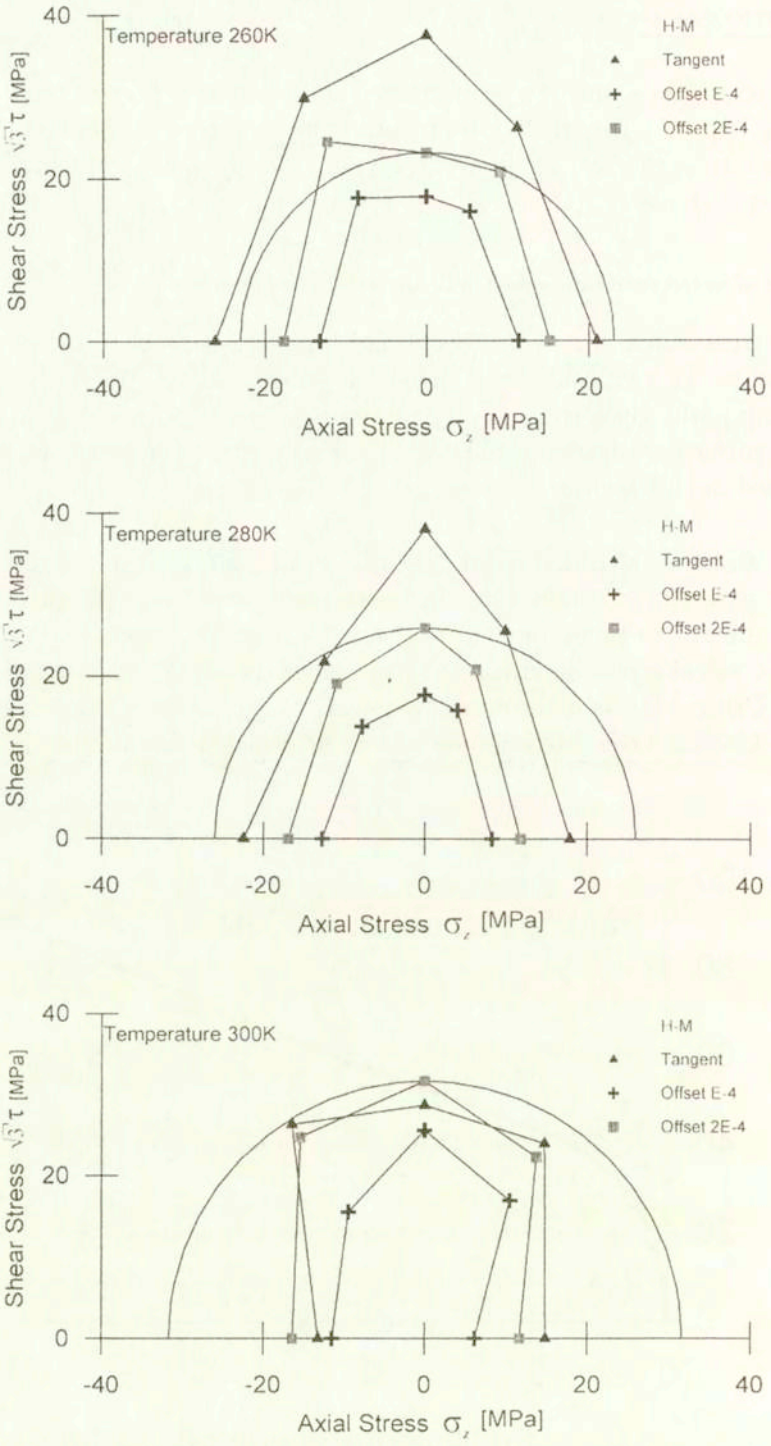

FIG. 11. Limit curve of reorientation exhibiting dependence of definition at: a) 260 K, b) 280 K and c) 300 K.

http://rcin.org.pl

3.6.2. Obtained results. Critical reorientation effective stresses are plotted in Fig. 11 at each test temperature. The normalized Huber-Mises curve is also drawn in the figure.

The result reveals firstly the strong dependence on the definition of critical stress, as is so for the yield surface in plasticity [41]. In the case of martensitic transformation in SMAs, according to the data in TiNi SMA [50], Cu-based SMA [44 – 47] and Fe-based SMA [48, 49], the transformation start stress in compression is larger than the one in tension. This asymmetry of the limit curve with respect to the shear stress-axis is also observed in the present result, though not so clearly. More experimental data should be accumulated to conclude whether or not this is an intrinsic property of SMAs in the reorientation processes of R-phase. However, it can be noticed that the shear critical stress (effective stress) is always higher than the axial critical stresses (tension, compression) on the $\sigma_z - \sqrt{3}\tau$ plane. This tendency is observed for all definitions of the critical stress intensities.

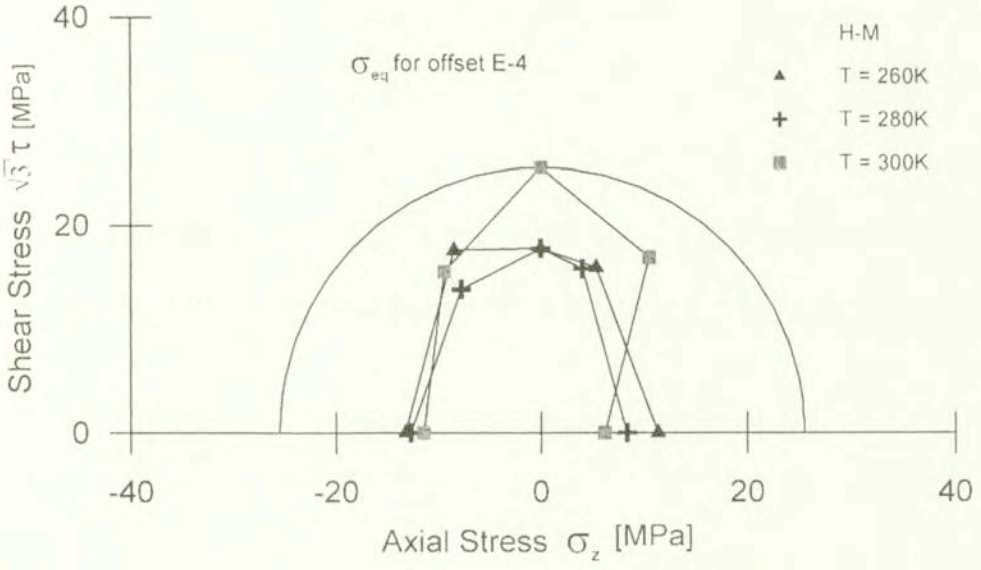

FIG. 12. Temperature-dependence of limit curve (offset 10^{-4}).

Figure 12 illustrates the temperature-dependence of the limit curve determined by the offset strain 10^{-4}. The data are replotted in Fig. 13 to compare the temperature sensitivity of the effective critical reorientation stress for each loading path. The lines represent the start line of the reorientation process of R-Phase [38 – 340, 59 – 60], about which MIYAZAKI *et al.* have discussed in detail under tension in TiNi alloys [54 – 56]. Linear relation with a negative slope and relatively high value of the critical stress in the present alloy, being similar

http://rcin.org.pl

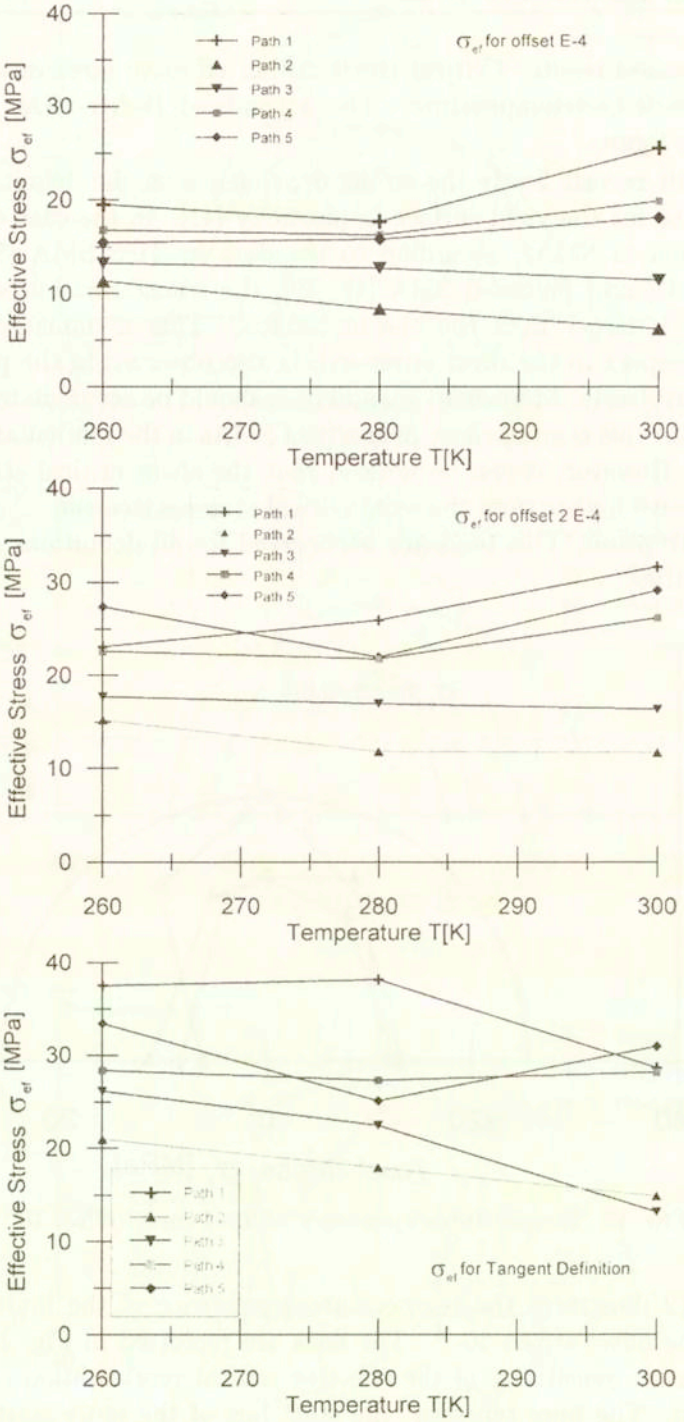

FIG. 13. Temperature sensitivity of critical reorientation stress determined by: a) offset strain 10^{-4}, b) offset strain $2 \cdot 10^{-4}$ and c) tangent.

http://rcin.org.pl

to Miyazaki's data, can be explained by the presence of the precipitates, which have actually been introduced by alloy-designing the present alloy [57]. At all temperature range, the shear stress contributes to such alloy performance as the positive temperature-dependence of critical stress and the higher critical stress level.

3.6.3. Description of limit surface - shape function. The obtained experimental data concerning the limit surface will now be employed in the convenient theoretical framework. It is assumed that the effects of hydrostatic stress are negligible. To verify this assumption, further multiaxial tests with the additional internal pressure should be carried out. Under this assumption the parametric form of the equation of the limit surface is given in vector representation of the deviatoric stress by

$$\mathbf{S} = \sqrt{\frac{2}{3}}\sigma^T(\mathbf{N},T)\mathbf{N}; \qquad \mathbf{N} = \frac{S}{|\mathbf{S}|} = \frac{\mathbf{S}}{\sigma_{ef}}\sqrt{\frac{2}{3}},$$

(3.4)

$$\mathrm{tr}\mathbf{N} = 0, \qquad \mathrm{tr}\mathbf{N}^2 = 1,$$

where $\mathbf{N}$ stands for the unit vector along $\mathbf{S}$, and four independent components of $\mathbf{N}$ play the role of parameters. Equivalently, the limit surface (3.4) can be described by

(3.5) $$\sigma_{ef} - \sigma^T(\mathbf{N},T) = 0.$$

Assume that σ^T is an isotropic function of $\mathbf{N}$. Its most general representation is $\sigma^T = \sigma^T(y,T)$, where $y = \sqrt{6}\mathrm{tr}(\mathbf{N}^3)$. It can be shown that the quantity y coincides with the one discussed and specified for A-experiments in Sec. 2.3. It is expedient to express the function $\sigma^T(y,T)$ in the form

(3.6) $$\sigma^T = \frac{\sqrt{3}k(T)}{f(y,T)}, \qquad F = \sigma_{ef} - \sigma^T(y,T) = 0,$$

where the shape function $f(y,T)$ of the limit surface $F = 0$ is normalized such that $f(0,T) = 1$, meaning that $k(T)$ stands for the critical shear stress. The values of the shape function can now be found from

(3.7) $$f(y,T) = \frac{\sigma^T(0,T)}{\sigma^T(y,T)},$$

The actual values of y for Paths #4 and #5 at each test temperature are given in Table 2, where $y_{0.1}$, $y_{0.2}$ and y_M denote the y values at the instant of the offset strains 10^{-4} and 2×10^{-4} and at the end of loading, respectively. The corresponding values of the shape function are collected on the plots shown in Fig. 14, for the case of the offsets 10^{-4} and 2×10^{-4}, at each test temperature.

http://rcin.org.pl

Table 2. Values of y-parameter.

Path Nr. (i)	Temp	260	280	300
	$y_{0.1}$	0.464	0.367	0.718
4	$y_{0.2}$	0.572	0.423	0.716
	y_M	0.6875	0.6568	0.6875
	$y_{0.1}$	−0.611	−0.677	−0.709
5	$y_{0.2}$	−0.629	−0.675	−0.719
	y_M	−0.6875	−0.6875	−0.6875

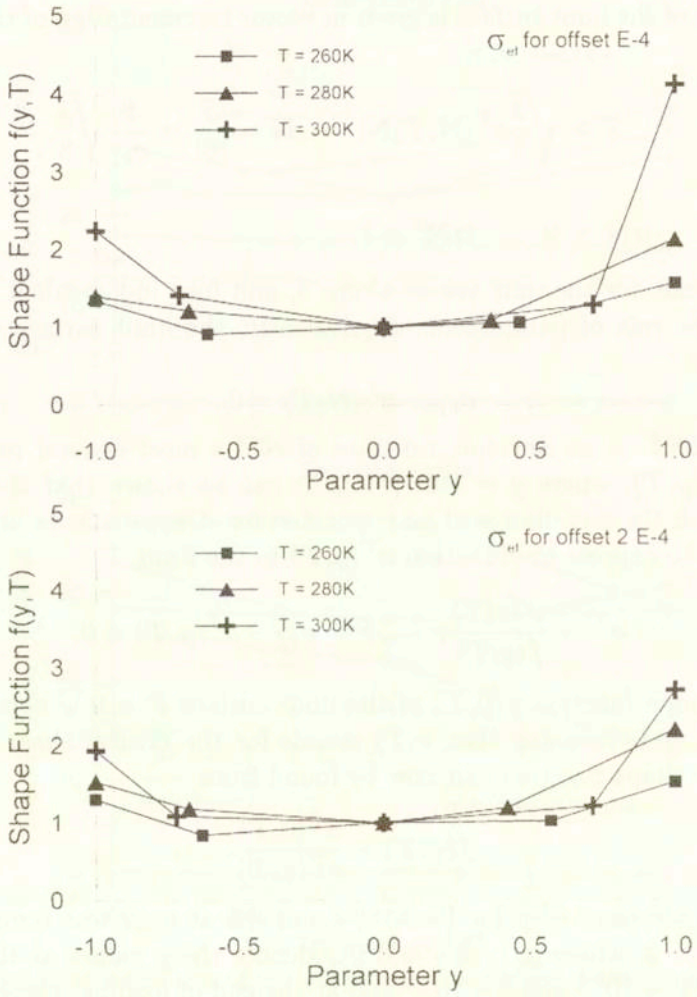

FIG. 14. Effect of temperature on shape function $f(y,T)$ determined by: a) offset strain 10^{-4} and b) offset strain 2×10^{-4}.

http://rcin.org.pl

It should be noted that $f(y,T) = 1$ corresponds to the J_2-theory in plasticity. It can easily be seen that the behaviour of the investigated alloy is described more accurately by the J_3-theory. Figure 14 also shows the definite temperature sensitivity of the shape function for the present alloy. In the case of martensitic transformation in Fe-based SMA, TANAKA *et al.* presented the data described by an almost temperature-independent shape function [61].

3.7. Some general properties of the plastic flow associated with the reorientation of R-phase

The experimental digital data have been further processed to display some general features of the deformation behaviour associated with the reorientation of the R-phase. On the theoretical ground they are most frequently grasped by the incremental permanent strain-stress relations (flow rule). The results are discussed in the subsequent subsections.

3.7.1. Homogeneity of flow rule.

i) We take it for granted that the reorientation process is rate-independent. Thus, the flow rule is supposed to be invariant under the change of the time scale. The fairly general and simplest flow rule that satisfies this requirement in the course of monotonic loading is

$$\dot{\varepsilon}^T_{ij} = \dot{\Lambda} G_{ij}(\sigma_{mn}, T), \qquad \dot{\Lambda} > 0, \tag{3.8}$$

where $\dot{\Lambda}$ is, in general, a positive scalar function of stress rate, temperature rate, parameters representing the history of $\boldsymbol{\sigma}, T$, and details of the reorientation process. During monotonic loading it represents the extent of the reorientation. The function $\mathbf{G}$ is assumed to be scaled so that it is a homogeneous function of the order zero with respect to σ,

$$G_{ij}(\tau\sigma^0_{mn}, T) = G_{ij}(\sigma^0_{mn}, T), \qquad \tau > 0. \tag{3.9}$$

Equations (3.8) – (3.9) incorporate all isotropic-hardening models of the usual mechanics of plastic flow. Moreover, many postulated constitutive equations for transformation strain in mechanics of phase transformation have the analytical form similar to Eqs. (3.8) – (3.9) [14, 20, 62 – 63].

The general character of the variation of $\dot{\Lambda}$ in the course of reorientation of R-phase can be deduced from Fig. 15, which shows the observed typical variation of the equivalent reorientation strain rate under increase of the applied effective stress. The presented curve clearly reveals that the reorientation process is governed by the "nucleation and growth" mechanism. The data in Fig. 15 and other similar results will be used in future research of evolution equation for Λ.

http://rcin.org.pl

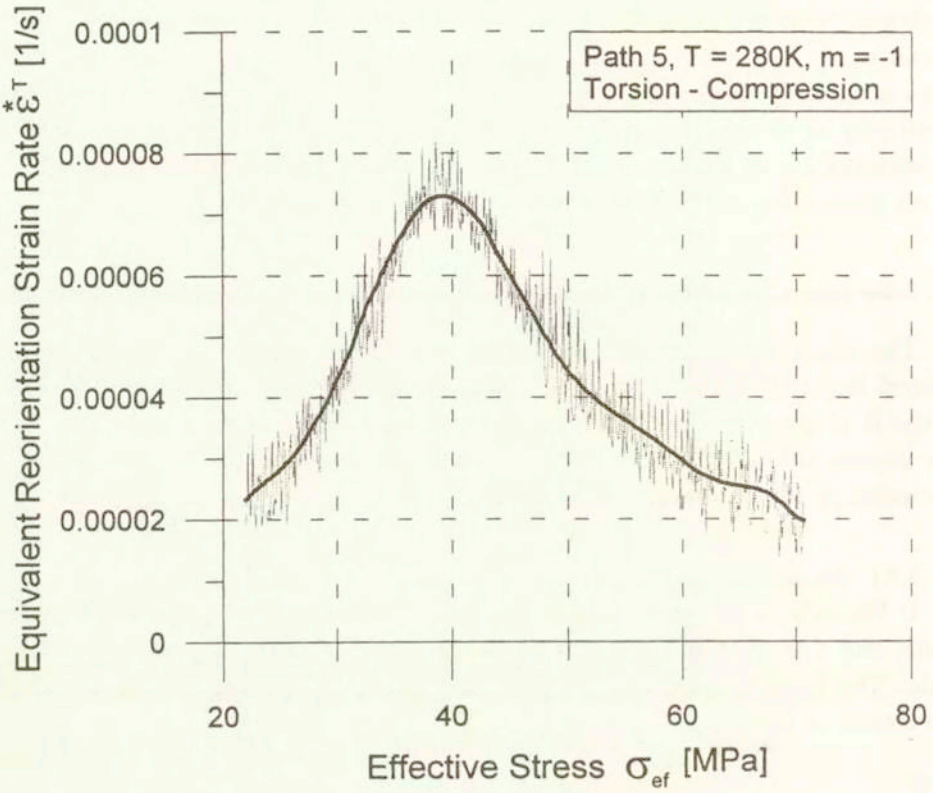

FIG. 15. Evolution of equivalent reorientation strain rate.

ii) The mathematical property (3.9) suggests that the reaction to the proportional loading is the proportional reorientation straining. Equivalently, it implies that the ratios of induced reorientation strain rates remains constant during reorientation,

$$\dot{\varepsilon}^{T}_{KL} = C\dot{\varepsilon}^{T}_{MN}; \qquad (K,L) \neq (M,N); \qquad C = \text{const}, \tag{3.10}$$

or, after integration over time,

$$\varepsilon^{T}_{KL} - \varepsilon^{offset}_{KL} = C(\varepsilon^{T}_{MN} - \varepsilon^{offset}_{MN}). \tag{3.11}$$

Thus the following formulas holds:

$$\frac{\dot{\varepsilon}^{T}_{KL}}{\dot{\varepsilon}^{T}_{MN}} = \frac{\varepsilon^{T}_{KL} - \varepsilon^{offset}_{KL}}{\varepsilon^{T}_{MN} - \varepsilon^{offset}_{MN}}. \tag{3.12}$$

The variation of ratios of reorientation strain rates at $T = 280$ K are shown in Fig. 16 for Path #5, and at $T = 260$ K in Fig. 17 for Path #4. It is seen that

http://rcin.org.pl

a)

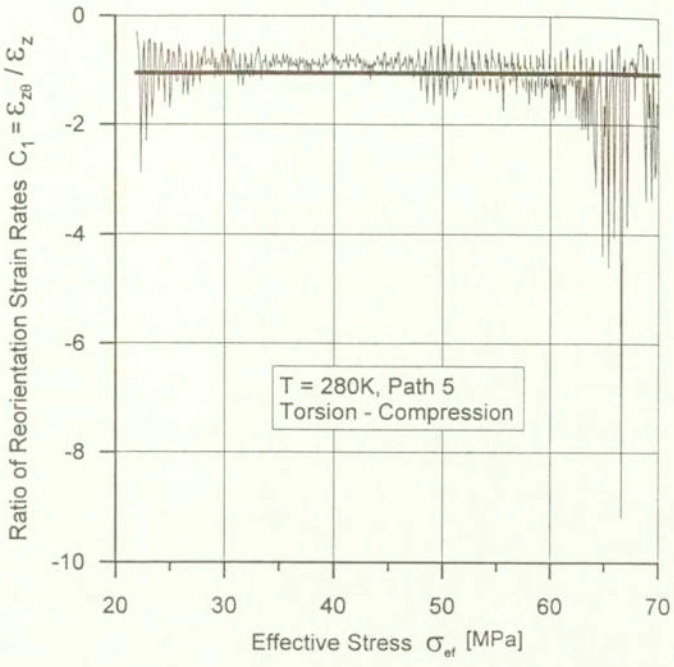

b)

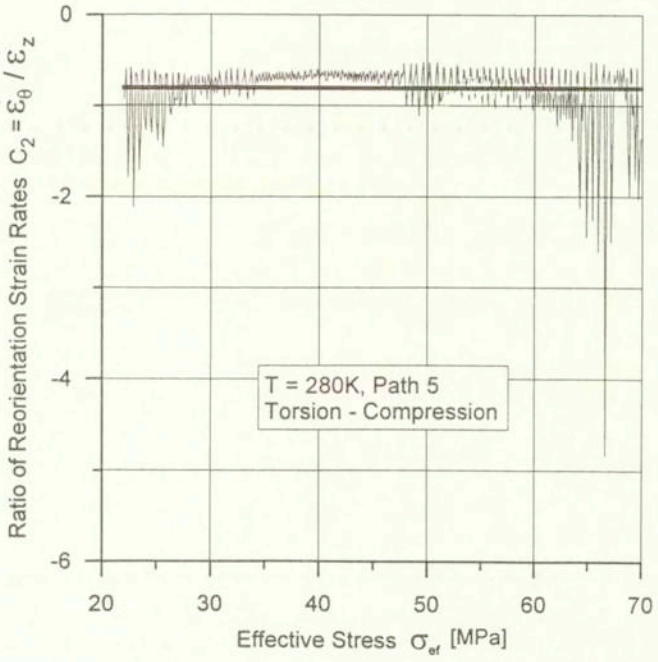

FIG. 16. Ratio of reorientation strain rates; a) and b).

http://rcin.org.pl

a)

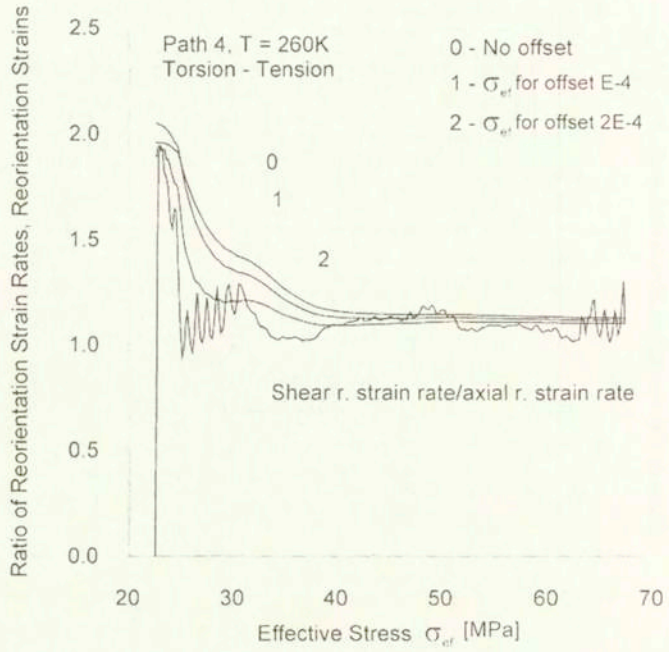

b)

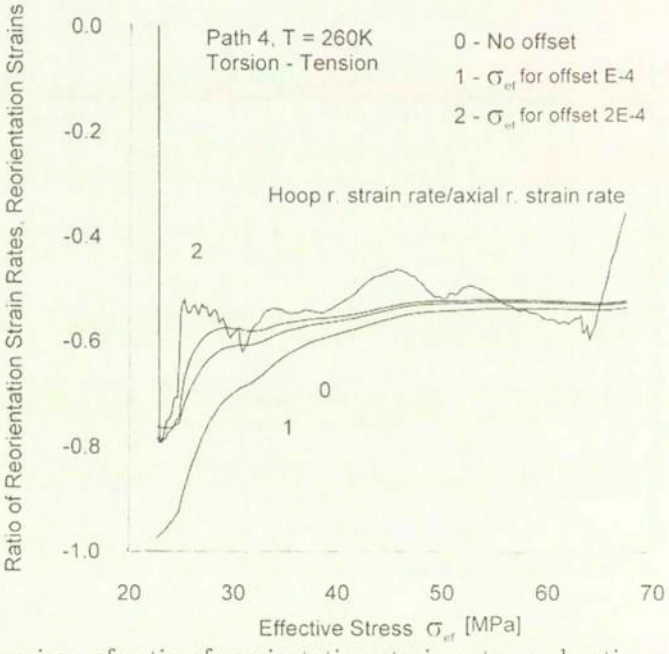

FIG. 17. Comparison of ratio of reorientation strain rates and ratios of reorientation strains for Path #4, $T = 260$ K; a) and b).

http://rcin.org.pl

the numerical data oscillate along a constant level. The mean values determine the constants $C_1 = \dot{\varepsilon}^T_{z\theta}/\dot{\varepsilon}^T_z$ and $C_2 = \dot{\varepsilon}^T_\theta/\dot{\varepsilon}^T_z$. In Fig. 17, the measured ratios of reorientation strains are plotted in addition, for different values of strain offset. The observed discrepancies between the curves in the initial stage of loading (that show disagreement with Eq. (3.12)) cannot be easily interpreted. The numerically calculated values of ratios are uncertain in the situation when numerators and denominators are close to zero. However, the curves quickly converge to the common constant value showing the trend of the behavior, which is in accord with Eq. (3.12). Interesting is the observed fading memory effect of the strain offsets.

3.7.2. Verification of the special isotropic flow rule.

i) Rewrite the equation of the limit surface $F = 0$ (cf. Eq. (3.6)) in the form

$$g_0^* = f(y,T)\sigma_{ef} - \sqrt{3}k(T) = 0,$$

and regard the function g_0^* as a potential for $\dot{\varepsilon}^T$;

$$\dot{\boldsymbol{\varepsilon}}^T = \dot{\Lambda}\frac{\partial g_0^*}{\partial \mathbf{S}} = \dot{\Lambda}_0\left[\frac{\mathbf{S}}{\sigma_{ef}} + 3x\left(3\frac{\mathbf{S}^2}{\sigma_{ef}^2} - \frac{2}{3}\mathbf{1} - y\frac{\mathbf{S}}{\sigma_{ef}}\right)\right], \tag{3.13}$$

where x and $\dot{\Lambda}_0$ are

$$x \equiv \frac{1}{f}\frac{\partial f}{\partial y} \quad \text{and} \quad \dot{\Lambda}_0 = \frac{3}{2}f\dot{\Lambda},$$

and $\mathbf{1}$ is the unit tensor.

It is seen that the flow rule written in the form (3.13) is the homogeneous function of order 0 in $\mathbf{S}$. Under the adopted simplifications (effects of hydrostatic stress are negligible, and $\mathrm{tr}(\dot{\boldsymbol{\varepsilon}}^T) = 0$), the term occurring in the bracket on the right-hand side of Eq. (3.13) is the most general representation of the isotropic tensor function $\mathbf{G}$, provided that x and y are independent scalar functions of the second and third invariant of $\mathbf{S}$. The adopted potentiality of the flow rule imposes merely the definite relationship between x and y presented above. The case $x = 0$ implies $f = \text{const.}$ and corresponds to the J_2-theory. The situation when x is not equal to zero will be referred to as the J_3-theory.

ii) Simple inspection of the mathematical structure of Eq. (3.13) shows that five components of $\dot{\boldsymbol{\varepsilon}}^T$ are expressed in terms of 3 scalars $\dot{\Lambda}$, x and y. This suggests that there may exists, in general, two constraint relations linking components of $\dot{\boldsymbol{\varepsilon}}^T$ and stress components, which are independent of the aforementioned 3 scalars. In the case of A-experiments discussed here, one constraint relation can be derived. Combine Eqs. (3.13) and (2.4) and get for the discussed specific case of stress and strain states

http://rcin.org.pl

$$\dot{\varepsilon}^T_{z\theta}/\dot{\varepsilon}^T_z = \frac{3}{2}\left[1 - \frac{3\tau^2 x}{M}\right]\frac{\tau}{\sigma_z},$$

(3.14)

$$\dot{\varepsilon}^T_{\theta}/\dot{\varepsilon}^T_z = -\frac{1}{2}\left[1 - \frac{9\tau^2 x}{M}\right],$$

where M is defined as

$$M = x\left(2\sigma_z^2 + 3\tau^2 - 2y\sigma_z\sigma_{ef}\right) + \frac{2}{3}\sigma_z\sigma_{ef}.$$

Elimination of x/M from Eq. (3.14) gives the final form of the constraint relation

$$\sigma_z\dot{\varepsilon}^T_{z\theta} + \tau\left(\dot{\varepsilon}^T_{\theta} - \dot{\varepsilon}^T_z\right) = 0,$$

which can be rewritten as follows:

$$Y = m = \frac{\tau}{\sigma_z}, \qquad Y = \frac{\dot{\varepsilon}^T_{z\theta}/\dot{\varepsilon}^T_z}{1 - \left(\dot{\varepsilon}^T_{\theta}/\dot{\varepsilon}^T_z\right)}. \tag{3.15}$$

Thus, in the course of A-experiments the measurable quantity Y should be equal to the stress ratio m, provided that the sample is isotropic and has the flow rule of the type (3.13). This theoretical prediction seems to be not exploited in the experimental mechanics so far. The measured and calculated values of Y are compared in Fig. 18. The result markedly verifies the theoretical prediction $Y = m$. In addition, in Table 3, we have collected the means of the strain rate ratios measured over the reorientation plateau. They are compared with the theoretical predictions of J_2- and J_3-theories. In the case of J_3-theory the theoretical values of x were chosen such that the theoretical ratios $\dot{\varepsilon}^T_{z\theta}/\dot{\varepsilon}^T_z$ are possibly closest to the measured values of the corresponding ratios for Paths #4 and #5. The measured data presented in Table 3 for Path #2 (tension), #3 (compression) and Path #1 (torsion) show substantial cross effects. Noticeably shear strain is induced during tension (compression), and large extension accompanies torsion. The former effect cannot be described by the J_3-theory at all (cf. Eq. $(3.14)_1$), and it certainly reveals the existing anisotropy. The cross effects are also present in the course of Paths #4 and #5. The disturbances they cause explain the deviations of the measured data from the straight line present in Fig. 18. However, one can conclude that the J_3-theory discussed here is more realistic than the J_2-theory.

iii) The qualitative agreement between experimental trends and theoretical predictions implied by Eq. (3.13) is also found when comparing the mean rate of reorientation work $W^* = S_{ij}\dot{\varepsilon}^T_{ij}$. The typical processed experimental data for dimensionless quantity $W^*/\sigma_{ef}\dot{\bar{\varepsilon}}^T$ are plotted versus effective stress in Fig. 19

http://rcin.org.pl

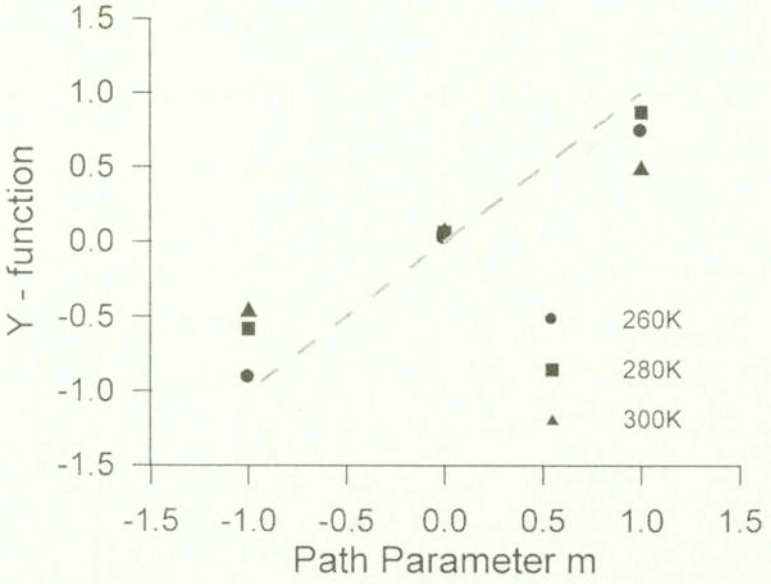

FIG. 18. Validation of constraint relation; Path-dependence of Y-function.

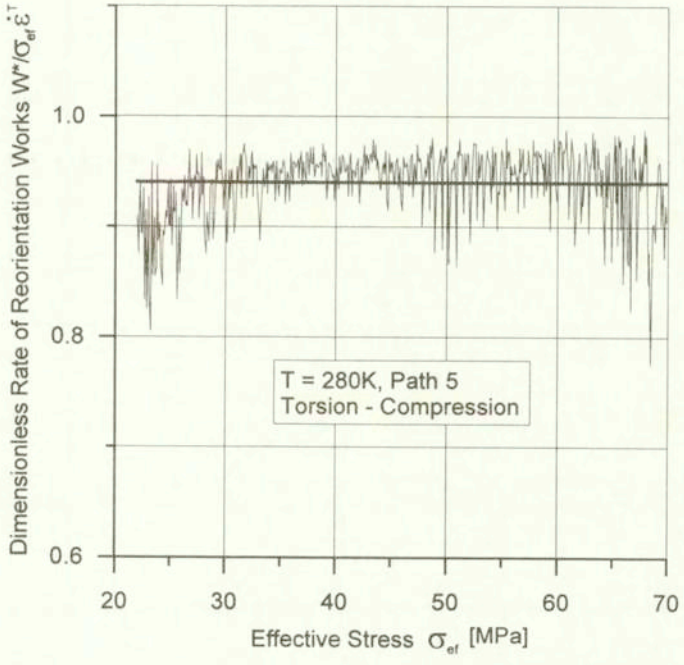

FIG. 19. Evolution in ratio of rate of reorientation works.

http://rcin.org.pl

Table 3. Comparison of measured and theoretical ratios of strain rates at: a) 260 K, b) 280 K and c) 300 K.

T = 260K

Paths			2	3	4	5	1	
Ratios			Tension	Compression	Tension + Torsion	Compression + Torsion	Torsion	Ratios of $\dot{\underline{\varepsilon}}$ for Torsion
$\dot{\varepsilon}_{z\theta}^T / \dot{\varepsilon}_z^T$	Exp.		0.03	0.06	1.14	-1.67	0.024	$\dot{\varepsilon}_z^T / \dot{\varepsilon}_{z\theta}^T$
	Theo.	J_3	0	0	1.14	-1.67	0.044	
		J_2	0	0	1.5	-1.5	0	
$\dot{\varepsilon}_\theta^T / \dot{\varepsilon}_z^T$	Exp.		-0.63	-0.52	-0.54	-0.84	0.064	$\dot{\varepsilon}_\theta^T / \dot{\varepsilon}_{z\theta}^T$
	Theo.	J_3	-0.5	-0.5	-0.14	-0.67	0.044	
		J_2	-0.5	-0.5	-0.5	-0.5	0	
$x = f'/f$			-	-	0.13	0.046	0.025	
Y			1	-1	11/16	-11/16	0	

T = 280K

Paths			2	3	4	5	1	
Ratios			Tension	Compression	Tension + Torsion	Compression + Torsion	Torsion	Ratios of $\dot{\underline{\varepsilon}}$ for Torsion
$\dot{\varepsilon}_{z\theta}^T / \dot{\varepsilon}_z^T$	Exp.		0.098	0.03	1.43	-1.05	0.73?	$\dot{\varepsilon}_z^T / \dot{\varepsilon}_{z\theta}^T$
	Theo.	J_3	0	0	1.43	-1.05	0	
		J_2	0	0	1.5	-1.5	0	
$\dot{\varepsilon}_\theta^T / \dot{\varepsilon}_z^T$	Exp.		-0.73	-0.53	-0.64	-0.8	-0.38	$\dot{\varepsilon}_\theta^T / \dot{\varepsilon}_{z\theta}^T$
	Theo.	J_3	-0.5	-0.5	-0.43	-0.05	0	
		J_2	-0.5	-0.5	-0.5	-0.5	0	
$x = f'/f$			-	-	0.02	-0.17	0	
Y			1	-1	11/16	-11/16	0	

T = 300K

Paths			2	3	4	5	1	
Ratios			Tension	Compression	Tension + Torsion	Compression + Torsion	Torsion	Ratios of $\dot{\underline{\varepsilon}}$ for Torsion
$\dot{\varepsilon}_{z\theta}^T / \dot{\varepsilon}_z^T$	Exp.		0.02	0.17	0.86	-0.87	0.33	$\dot{\varepsilon}_z^T / \dot{\varepsilon}_{z\theta}^T$
	Theo.	J_3	0	0	1.01	-1.01	0	
		J_2	0	0	1.5	-1.5	0	
$\dot{\varepsilon}_\theta^T / \dot{\varepsilon}_z^T$	Exp.		-1.45	-1.14	-0.72	-0.94	0	$\dot{\varepsilon}_\theta^T / \dot{\varepsilon}_{z\theta}^T$
	Theo.	J_3	-0.5	-0.5	0	0	0	
		J_2	-0.5	-0.5	-0.5	-0.5	0	
$x = f'/f$			-	-	0.19	-0.19	0.025	
Y			1	-1	11/16	-11/16	0	

http://rcin.org.pl

for Path #5 and $T = 280$ K. They oscillate around a constant level that can be identified with a mean value. This experimental trend is in agreement with the property discussed in Sec. 3.7.1. The mean values of the experimental dimensionless rate of reorientation work are presented for different paths and temperatures on a single diagram shown in Fig. 20. They are all lesser than unity – the common value, which predicts the J_2-theory. In the case of J_3-theory, for considered A-experiments, the effective reorientation strain rate and dimensionless rate of reorientation work can be calculated by means of Eqs. (3.3) and (2.2). The result is

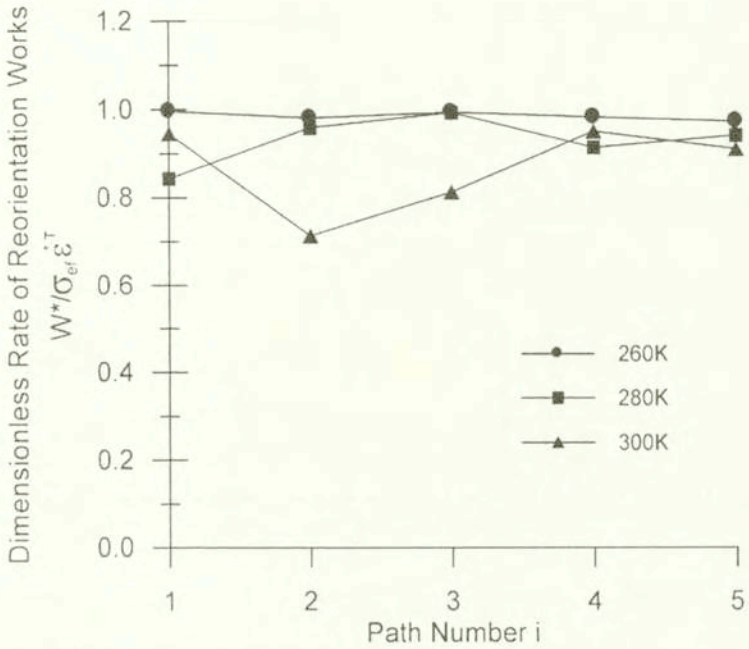

FIG. 20. Path-dependence of dimensionless rate of reorientation work.

$$\dot{\varepsilon}^T = f\dot{\Lambda}\left[1 + 9x^2(1-y^2)\right]^{1/2}, \tag{3.16}$$

$$\frac{W^*}{\sigma_{ef}\dot{\varepsilon}^T} = \frac{1}{\left[1 + 9x^2(1-y^2)\right]^{1/2}} \tag{3.17}$$

The calculated (with use of Eq. (3.17)) theoretical results are given in Table 4 for x values given in Table 3. It is interesting that the calculated values for Paths #4 and #5 are smaller than 1. This shows that account for the third invariant in a theoretical model slightly improves the quality of predictions.

http://rcin.org.pl

Table 4. Theoretical values of dimensionless rate of reorientation work.

Temp	Path	1	2	3	4	5
	y	0	1	-1	11/16	$-11/16$
260	$W^*/\sigma_{ef}\varepsilon^{*T}$	0.997	1	1	0.962	0.995
280		1	1	1	0.999	0.938
300		1	1	1	0.924	-0.924

The observed discrepancies are again due to existence of the cross-effects. Certain influence stems also from the fact that actual paths deviate from the proportional one as shown in Fig. 3 and remarked in Sec. 3.1.

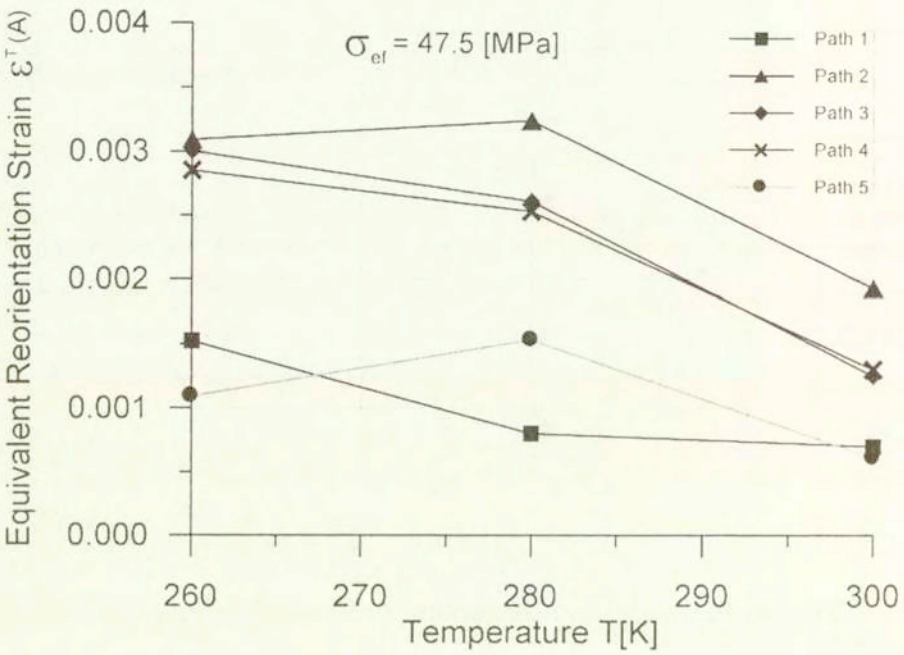

FIG. 21. Equivalent reorientation strain crresponding to $\sigma_{ef} = 47.4$ MPa.

3.8. The range of straining

As already remarked in Sec. 3.1, the maximum stresses were different for different paths and T. The minimum value equal to 47.5 MPa of the effective stress was achieved for Path #2 and $T = 280$ K. This value of the effective stress produces different equivalent reorientation strains along different paths. They are denoted by $\varepsilon^T(A)$ and collectively presented in Fig. 21. The corresponding permanent equivalent reorientation strains (that could be obtained after unload-

http://rcin.org.pl

ing) are denoted by $\varepsilon^T(B)$. Their approximate values are obtained by "parallel" transition of the measured unloading curves that start from the maximum value of the applied effective stress for given path and temperature. They are given in Fig. 22. The presented data leads to the conclusion, which have already been drawn in Sec 3.5 that (for fixed equivalent stress) the equivalent strains in pure shear or combined shear and compression are the smallest.

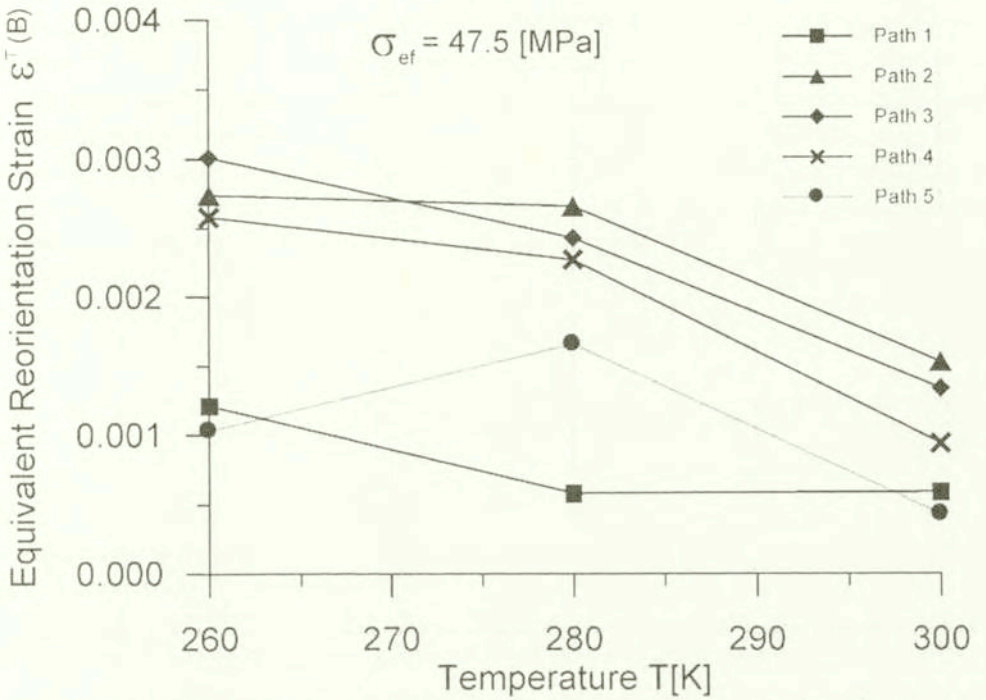

FIG. 22. Permanent equivalent reorientation strain obtained after unloading from $\sigma_{ef} = 47.4$ MPa.

4. Concluding remarks

The deformation behaviour associated with the R-phase reorientation was investigated in a Ti-51.0at%Ni polycrystalline shape memory alloy under the torsion-tension (compression) stress state, and a continuum mechanical approach was proposed to describe the alloy performance.

The limit condition to start the reorientation process, represented as a surface on the axial stress-shear stress plane, was determined for the proportional loading path, and was shown to be not described by the Huber-Mises condition (the J_2-theory). A theoretical framework was presented to model the actual limit surface by taking into account the third invariant of stress deviator through the concept of the shape function. The values of the shape function were experimentally

http://rcin.org.pl

determined, revealing clearly its path- and temperature-dependence.

The basic experimental features of the plastic flow in the R-phase, such as the flow rule, the ratios of the reorientation strain rates and the dimensionless ratio of the reorientation work, were compared with the predictions of theories that neglect the effects of pressure, compressibility of reorientation strains and effects of induced anisotropy.

The experimental trends qualitatively confirm the predictions of both the J_2-theory and the J_3-theory. The introduction of the third invariant of stress deviator into the theoretical framework improves quantitative discrepancies. However, the macroscopic (overall) deformations accompanying the internal reorientation must be strongly influenced by the second order internal stresses generated in the processes. Therefore, better description should use an extra tensorial parameter representing the internal stresses. The kinematical hardening models, with the back stress as an additional variable, are expected to be more adequate for the description of the flow associated with detwinning. Such models would enable us to describe the experimental trends caused by the induced anisotropy observed here.

Acknowledgments

The authors are grateful for the alloy supply by Mr. T.Ueki and for preparation of the specimens by Messrs. M. Taira, M. Kadowaki and H. Kikuchi.

This work was financially supported by the Polish State Committee for Scientific Research through the research program KBN Nr.7T07A00513. The financial aid by the Japan Society of Promotion of Sciences through the Japan-Europe Research Cooperative Program is also acknowledged.

References

1. S. MIYAZAKI, K. NONURA and A. ISHIDA, *Shape memory effects associated with the martensitic and R-phase transformations in sputtered-deposited TiNi thin films*, J. Phys. IV, coll.5-8, 677–682, 1995.
2. M. FREMOND and S. MIYAZAKI [Eds.], *Shape memory alloys*, Springer-Verlag, Wien-New York 1996.
3. K.D. SKROBANEK, M. KOHL and S. MIYAZAKI, *Stress-optimised shape memory microactuator*, Proc. 3rd ICIM/ECSSM '96, Lyon 1996.
4. Y. MORIYA, H. KIMURA, S.ISHIZAKI, S. HASHIZUME, S. SUZUKI, H. SUZUKI and T. SAMPEI, *Properties of Fe-Cr-Ni-Mn-Si (-Co) shape memory alloys*, J. Phys. IV, coll.1-4, 433–438, 1991.
5. V. BIRMAN, *Review of mechanics of shape memory alloy structures*, Appl. Mech. Rev., **50**, 629–645, 1997.

http://rcin.org.pl

6. E.P. GEORGE, R. GOTTHARDT, K. OTSUKA, S. TROLIER-MOKINSTRY and M. WUN-FOGLE [Eds.], *Materials for smart systems* II, Materials Research Society, Pittsburg 1997.

7. Z.G. WEI, R. SANDSTRÖM and S. MIYAZAKI, *Shape-memory materials and hybrid composites for smart systems*, Part I and II, J. Materials Sci., **33**, 3743–3762, 3763–3783, 1998.

8. F. FALK, *Model free energy, mechanics, and thermodynamics of shape memory alloys*, Acta Metall., **28**, 1773–1780, 1980.

9. F. FALK, *One-dimensional model of shape memory alloys*, Arch. Mech., **35**, 63–84, 1983.

10. K. TANAKA, *A thermomechanical sketch of shape memory effect: One-dimensional tensile behavior*, Res. Mech., **18**, 251–263, 1986.

11. K. TANAKA, S. KOBAYASHI and Y. SATO, *Thermomechanics of transformation pseudoelasticity and shape memory effect in alloys*, Int. J. Plasticity, **2**, 59–72, 1986.

12. I. MÜLLER, *On the size of the hysteresis in pseudoelasticity*, Continuum Mech. Thermodyn., **1**, 125–142, 1989.

13. I. MÜLLER and HUIBIN XU, *On the pseudo-elastic hysteresis*, Acta Metall. Mater., **39**, 263–271, 1991.

14. B. RANIECKI, CH. LEXCELLENT and K. TANAKA, *Thermodynamic model of pseudoelastic behaviour of shape memory alloys*, Arch. Mech., **44**, 261–248, 1992.

15. B. RANIECKI and CH. LEXCELLENT, *R-models of pseudoelasticity and their specification for some shape memory solids*, Euro. J. Mech., A/Solids, **13**, 21–50, 1994.

16. B. RANIECKI and CH. LEXCELLENT, *Thermodynamics of isotropic pseudoelasticity in shape memory alloys*, Euro. J. Mech. A/Solids, **17**, 185–205, 1998.

17. C. LIANG and C.A. ROGERS, *One-dimensional thermomechanical constitutive relations for shape memory materials*, J. Intell. Mater. Syst. Struct., **1**, 207–234, 1990.

18. X.D. ZHANG, C.A. ROGERS and C. LIANG, *Modelling of the two-way shape memory effect*, Phil. Mag. A, **65**, 1199–1215, 1992.

19. L.C. BRINSON and R. LAMMERING, *Finite element analysis of the behavior of shape memory alloys and their applications*, Int. J. Solids Struct., **30**, 3261–3280, 1993.

20. Q.P. SUN and K.C. HWANG, *Micromechanics modelling for the constitutive behavior of polycrystalline shape memory alloys* – I. II, J. Mech. Phys. Solids, **41**, 1–17, 19–33, 1993.

21. V. KAFKA, *Shape memory: A new concept of implementation and of mathematical modelling*. Part I and II, J. Intell. Mater. Syst. Struct., **5**, 809–814, 815–824, 1994.

22. Y. IVSHIN and T.J. PENCE, *A constitutive model for hysteretic phase transition behavior*, Int. J. Engng Sci., **32**, 681–704, 1994.

23. R.D. SPIES, *Results on a mathematical model of thermomechanical phase transitions in shape memory materials*, Smart Mater. Sturct., **3**, 459–469, 1994.

24. E.J. GRAESSER and F.A. COZZARELLI, *A proposed three-dimensional constitutive model for shape memory alloys*, J. Intell. Mater. Syst. Struct., **5**, 78–89, 1994.

25. V.I. LEVITAS, *The postulate of realizability: Formulation and applications to the post-bifurcation behaviour and phase transitions in elastoplastic materials* – I, II, Int. J. Engng Sci., **33**, 921–945, 947–971, 1995.

26. E.N. MAMIYA and J.C. SIMO, *Stress-induced phase transformations in elastic solids under anti-plane deformations: dissipative constitutive models and numerical simulation*, Computer Methods Appl. Mech. Engng, **133**, 47–77, 1996.

http://rcin.org.pl

27. F. AURICCHIO, R.L. TAYLOR and J. LUBLINER, *Shape-memory alloys: macromodelling and numerical simulations of the superelastic behavior*, Computer Methods Appl. Mech. Engng, **146**, 281–321, 1997.

28. F.D. FISCHER, E.R. OBERAIGNER, K. TANAKA and F. NISHIMURA, *Transformation induced plasticity revised: An update formulation*, Int. J. Solids Struct., **35**, 2209–2227, 1998.

29. S. LECLERCQ, C. LEXCELLENT and J.C. GELIN, *A finite element calculation of devices made of shape memory alloys*, J. Physique IV, Coll. C1, suppl. J. Physique III, **6**, 225–234, 1996.

30. A. ZIÓŁKOWSKI and B. RANIECKI, *FEM-based formulation of the coupled thermomechanical problems of shape memory alloys*, [in:] M. AAKIYAMA and M. KLEIBER [Eds.], Proceedings of the Japan-Central Europe Joint Workshop on Advanced Computing in Engineering, Pułtusk, September 26-29, 207–212, IPPT PAN, Warsaw 1994.

31. A. ZIÓŁKOWSKI and B. RANIECKI, *FEM-analysis of the one-dimensional coupled thermomechanical problem of TiNi SMA*, Suppl. J. Physique III, No. 1, c1, 395, 1996.

32. A. ZIÓŁKOWSKI, *On the layered medium with elastic and shape memory alloy plies under various loading rates*, [in:] O.T. BRUHNS and E. STEIN [Eds.], IUTAM-Symposium on Micro- and Macrostructural Aspects of Thermoplasticity, 427–436, Kluwer Academic Publishers, Dordrecht 1999.

33. E. PATOOR, A. EBERHARDT and M. BERVEILLER, *Thermomechanical behaviour of shape memory alloys*, Arch. Mech., **40**, 775–794, 1988.

34. F.D. FISCHER, *Modelling and simulation of transformation induced plasticity in elastoplastic materials*, [in:] M. BERVEILLER and F.D. FISCHER [Eds.], Mechanics of Solids with Phase Changes, Springer-Verlag, Wien-New York 1997.

35. H. FUNAKUBO, [Ed.], *Shape memory alloys*, Gordon and Breach Science Publishers, New York 1987.

36. T.W. DUERIG, K.M. MELTON, D. STÖCKEL and C.M. WAYMAN, *Engineering aspects of shape memory alloys*, Butterworth-Heinemann, London 1990.

37. F. NISHIMURA, N. WATANABE and K. TANAKA, *Analysis of uniaxial stress-strain-temperature hysteresis in an Fe-based shape memory alloy under thermomechanical loading*, Computational Mater. Sci., **8**, 349–362, 1997.

38. A. BEKKER and L.C. BRINSON, *Temperature-induced phase transformation in a shape memory alloy: Phase diagram based kinetics approach*, J. Mech. Phys. Solids, **45**, 949–988, 1997.

39. A. BEKKER and L.C. BRINSON, *Phase diagram based description of the hysteresis behavior of shape memory alloys*, Acta Mater. **46**, 3649–3665, 1998.

40. K. TANAKA, F. NISHIMURA, H. KATO and S. MIYAZAKI, *Transformation thermomechanics of R-phase in TiNi shape memory alloys*, Arch. Mech., **49**, 547–572, 1997.

41. J. LAMAITRE and J.-L. CHABOCHE, *Mechanics of solids materials*, Cambridge University Press, Cambridge 1990.

42. L. ORGEAS and D. FAVIER, *Non-symmetric tension-compression behaviour of NiTi alloy*, J. Phys., coll.**8**-5, 605–610, 1995.

43. L. ORGEAS and D. FAVIER, *Stress-induced martensitic transformation of a NiTi alloy in isothermal shear, tension and compression*, Acta Mater., **46**, 5579–5591, 1998.

44. M. TOKUDA, P. SITTNER, M. TAKAKURA and YE MEN, *Experimental study on performances in Cu-based shape memory alloy under multiaxial loading conditions*, Materials Sci. Research Int., **1**, 260–265, 1995.

http://rcin.org.pl

45. P. SITTNER and M. TOKUDA, *Reorientation in combined stress induced martensite?*, J. Phys., coll.**8**-5, 1003–1008, 1995.

46. P. SITTNER, Y. HARA and M. TOKUDA, *Experimental study on the thermoelastic martensitic transformation in shape memory alloy polycrystal induced by combined external forces*, Metall. Mater. Trans. A, **26A**, 2923–2935, 1995.

47. C. ROGUEDA, C. LEXCELLENT and L. BOCHER, *Experimental study of psudoelastic behaviour of a CuZnAl polycrystalline shape memory alloy under tension-torsion proportional and non-proportional loading tests*, Arch. Mech., **48**, 10250–1045, 1996.

48. F. NISHIMURA, N. WATANABE, T. WATANABE and K. TANAKA, *Transformation conditions in an Fe-based shape memory alloy under tensile-torsional loads: Martensite start surface and austenite start/finish planes*, Materials Sci. Engng A, **264**, 232–244 1999.

49. F. NISHIMURA, N. WATANABE and K. TANAKA, *Evolution of martensite start condition in general thermomechanical loads of an Fe-based shape memory alloy*, Int. J. Mech. Sci., 1999, in press.

50. K. JACOBUS, H. SEHITOGLU and M. BLAZER, *Effect of stress state on the stress-induced martensitic transformation in polycrystalline Ni-Ti alloy*, Metall. Mater. Trans. A, **27A**, 1–8, 1996.

51. K. GALL, H. SEHITOGLU, H.J. MAIER and K. JACOBUS, *Stress-induced martensitic phase transformations in polycrystalline CuZnAl shape memory alloys under different stress states*, Metall. Mater. Trans. A, **29A**, 763–773, 1998.

52. E. PATOOR, A. EBERHARDT and M. BERVEILLER, *Micromechanical modelling of the shape memory behavior*, [in:] L.C. BRINSON and B. MORAN [Eds.], Mechanics of phase transformations and shape memory alloys, AMD **189**/PVP **292**, ASME, 23–37, 1994.

53. K. OTSUKA and C.M. WAYMAN [Eds.], *Shape memory materials*, Cambridge University Press, Cambridge 1998.

54. S. MIAYZAKI and K. OTSUKA, *Deformation and transition behavior associated with the R-phase in Ti-Ni alloys*, Metall. Trans., A, **17A**, 53–63, 1986.

55. S. MIYAZAKI and C.M. WAYMAN, *The R-phase transition and associated shape memory mechanism in TiNi single crystals*, Acta Metall., **36**, 181–192, 1988.

56. S. MIYAZAKI, S. KIMURA and K. OTSUKA, *Shape-memory effect and pseudoelasticity associated with the R-phase transition in Ti-50.5 at.%Ni single crystals*, Phil. Mag. A, **57**, 467–478, 1988.

57. K. TANAKA, K. KITAMURA and S. MIYAZAKI, *Shape memory alloy preparation for multiaxial tests and identification of fundamental alloy performance*, see this issue of Arch. Mech. **51**, 6, 727–744, 1999.

58. B. RANIECKI, L. DIETRICH, Z.L. KOWALEWSKI, G. SOCHA, S. MIYAZAKI, K. TANAKA, *Experimental methodology fot TiNi shape memory alloy testing under complex stress state*, see this issue of Arch. Mech., **51**, 6, 727–744, 1999.

59. D.J. BARRETT, *A three-dimensional phase transformation model for shape memory alloys*, J. Intelligent Material Syst. Structures, **6**, 831–839, 1995.

60. H. TOBUSHI, S. YAMADA, T. HACHISUKA, A. IKAI and K. TANAKA, *Thermomechanical properties due to martensitic and R-Phase transformations of TiNi shape memory alloy subjected to cyclic loadings*, Smart Mater. Struct., **5**, 788–795, 1996.

61. K. TANAKA and T. WATANABE, *Transformation conditions in a Fe-based shape memory alloy: An experimental study*, Arch. Mech., to be submitted.

http://rcin.org.pl

62. J.B. LEBLOND, G. MOTTET and J.C. DEVAUX, *A theoretical and numerical approach to the plastic behaviour of steels during phase transformation* – I, II, J. Mech. Phys. Solids, **34**, 395–409, 411–432, 1986.

63. J.G. BOYD and D.C. LAGOUDAS, *A thermodynamical constitutive model for shape memory materials*, I, **12**, 805–842, 1996.

Received March 24, 1999.

http://rcin.org.pl